Joule

CellPress

Article

High Reversibility of Lattice Oxygen Redox Quantified by Direct Bulk Probes of Both Anionic and Cationic Redox Reactions

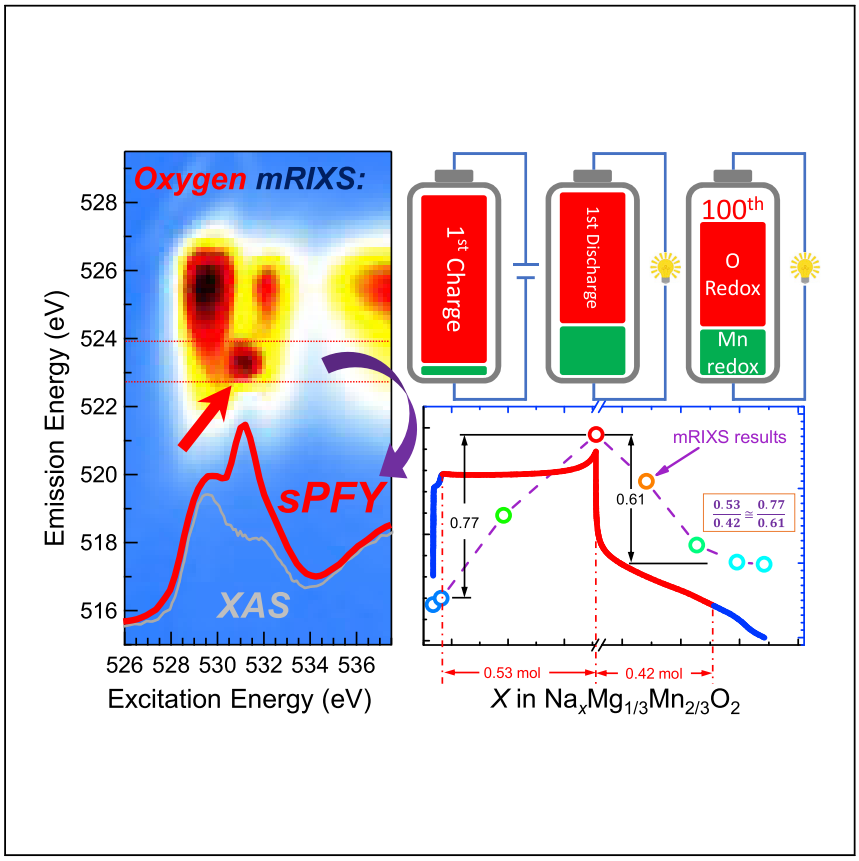

Reversibility of lattice oxygen redox holds the key to its practical employments, especially in 3*d* transition-metal compounds. Here, direct, independent, and quantitative bulk probes of both cationic and lattice anionic redox chemistry are achieved through mapping of resonant inelastic X-ray scattering. We found highly reversible lattice oxygen redox in $Na_{2/3}Mg_{1/3}Mn_{2/3}O_2$ (79%) and $Li_{1.17}Ni_{0.21}Co_{0.08}Mn_{0.54}O_2$ (76%) during the initial cycle, with 87% and 44% capacity retention after 100 and 500 cycles, respectively. Therefore, aside from other oxygen activities, lattice oxygen redox could be highly reversible in batteries.

Kehua Dai, Jinpeng Wu, Zengqing Zhuo, ..., Zahid Hussain, Gao Liu, Wanli Yang

gliu@lbl.gov (G.L.)
wlyang@lbl.gov (W.Y.)

HIGHLIGHTS

Direct quantifications of bulk transition-metal 3*d* and oxygen 2*p* redox states

Lattice O redox is 79% reversible and 87% sustained in 100-cycle $Na_{2/3}Mg_{1/3}Mn_{2/3}O_2$

Mn redox emerges during discharge and Mn^{2+} grows on surface upon cycling

Lattice O redox is 76% reversible in $Li_{1.17}Ni_{0.21}Co_{0.08}Mn_{0.54}O_2$

Dai et al., Joule 3, 518–541
February 20, 2019
https://doi.org/10.1016/j.joule.2018.11.014

Joule

CellPress

Article

High Reversibility of Lattice Oxygen Redox Quantified by Direct Bulk Probes of Both Anionic and Cationic Redox Reactions

Kehua Dai,[1,2,3] Jinpeng Wu,[2,4] Zengqing Zhuo,[2,5] Qinghao Li,[2,6] Shawn Sallis,[2,7] Jing Mao,[8] Guo Ai,[3,9] Chihang Sun,[1] Zaiyuan Li,[1] William E. Gent,[10] William C. Chueh,[11,12] Yi-de Chuang,[2] Rong Zeng,[13] Zhi-xun Shen,[4] Feng Pan,[5] Shishen Yan,[6] Louis F.J. Piper,[7] Zahid Hussain,[2] Gao Liu,[3,*] and Wanli Yang[2,14,*]

SUMMARY

The reversibility and cyclability of anionic redox in battery electrodes hold the key to its practical employments. Here, through mapping of resonant inelastic X-ray scattering (mRIXS), we have independently quantified the evolving redox states of both cations and anions in $Na_{2/3}Mg_{1/3}Mn_{2/3}O_2$. The bulk Mn redox emerges from initial discharge and is quantified by inverse partial fluorescence yield (iPFY) from Mn-*L* mRIXS. Bulk and surface Mn activities likely lead to the voltage fade. O-*K* super-partial fluorescence yield (sPFY) analysis of mRIXS shows 79% lattice oxygen redox reversibility during the initial cycle, with 87% capacity sustained after 100 cycles. In $Li_{1.17}Ni_{0.21}Co_{0.08}Mn_{0.54}O_2$, lattice oxygen redox is 76% initial-cycle reversible but with only 44% capacity retention after 500 cycles. These results unambiguously show the high reversibility of lattice oxygen redox in both Li-ion and Na-ion systems. The contrast between $Na_{2/3}Mg_{1/3}Mn_{2/3}O_2$ and $Li_{1.17}Ni_{0.21}Co_{0.08}Mn_{0.54}O_2$ systems suggests the importance of distinguishing lattice oxygen redox from other oxygen activities for clarifying its intrinsic properties.

INTRODUCTION

The pressing demand for battery technologies with high capacity, stability, and low cost calls for conceptual breakthroughs and material developments that could be commercially viable. Among the formidable challenges of improving almost every component in batteries, the transition-metal (TM) oxide-based cathode remains a bottleneck of the energy density and sits at the center of much research and development efforts. In a conventional wisdom, redox reactions associated with only the 3*d* valence states of the 3*d* TMs in oxide cathodes are desirable because involving oxygen in the electrochemical operation was considered detrimental to the reversibility and safety, mainly through the irreversible loss of oxygen and parasitic surface reactions. Such a consideration has directly triggered the innovations of TM oxide-based cathodes over chalcogenides, and successfully guided various cathode material developments that are currently employed for commercial batteries.[1] However, recent research on oxygen states in battery cathodes has indicated that lattice oxygen redox could be reversible and potentially practical for batteries with improved capacity and energy density.[2] Although the fundamental mechanism of O redox remains elusive and is under active debate between many scenarios, e.g., peroxide with shortened O-O distance,[3,4] general localized oxygen holes,[5]

Context & Scale

Battery cathodes based on 3*d*-transition-metal oxides need viable improvements in their energy density. Recent proposals of O redox have enabled conceptual possibilities, although the assessment of its reversibility remains elusive. This work reports independent and direct quantifications of the evolving O-2*p* and Mn-3*d* redox states through O-*K* and Mn-*L* mapping of resonant inelastic X-ray scattering (mRIXS). The high reversibility of the lattice O redox in $Na_{2/3}Mg_{1/3}Mn_{2/3}O_2$ (79%) and $Li_{1.17}Ni_{0.21}Co_{0.08}Mn_{0.54}O_2$ (76%) is revealed during the initial cycle. While $Na_{2/3}Mg_{1/3}Mn_{2/3}O_2$ displays decent O-redox capacity retention (87% after 100 cycles), the Li-rich system shows significant decay (44% after 500 cycles). We demonstrate direct quantifications of the reversibility of lattice O redox through photon-in-photon-out bulk-sensitive mRIXS. The quantification results directly show that the reversibility of lattice O redox could be very high in both Li-ion and Na-ion batteries.

structural configurations of alkali-rich and disordered systems,[6] and specific oxygen chemical bonds,[7] a number of claims of O redox have been made in both Li-ion batteries (LIBs) and Na-ion batteries (NIBs) (see a review by Assat and Tarascon[8] and many references therein).

While the concept of "reversible" O redox has been applied to many cathode materials, as summarized in multiple reviews,[7–9] one could easily notice a mismatch between the claimed "reversibility" and experimental findings. A majority of these previous studies is based on structural probes and hard X-ray absorption of TM *K*-edges, as indirect evidence of the oxygen chemistry. The popular O-*K* spectroscopy, especially X-ray photoelectron spectroscopy (XPS)[4,10,11] with probe depth of up to 30 nm with hard X-rays,[12] and X-ray absorption spectroscopy (XAS),[5,13–16] have been mostly reported for initial cycles, with only a few studies extended to the second cycle.[17,18] Quantifications of O redox during the first cycle have been performed based on the intensity of the pre-edge features of O-*K* XAS;[5,13,19] however, the results display obvious discrepancy with the electrochemical profile. For example, the O-redox quantification values display a significant increase even before the charge plateau of the Li-rich compounds.[5,13] In addition, compared with the initial charge process, the lower-capacity discharge process shows an even higher oxygen-reduction value.[5,13,19] Such discrepancy is due to the fact that intensities of O-*K* XAS pre-edge features are dominated by the TM-O hybridization, which enhances upon charging due to the oxidization of the system, so it is rather a probe of TM-O hybridization and does not follow the electrochemical profile on O redox itself.[20] As a matter of fact, the missing reliable experimental results for quantitatively assessing the reversibility of O redox have led to controversy. For example, manganese-based NIB cathode materials with low-valence dopants, $Na_yM_xMn_{1-x}O_2$ (x, $y \leq 1$, M = Ni, Mg, Li, etc.), have been reported with high volumetric energy density.[21–24] While reversible O redox has been claimed in several works without direct evidence over extended cycles, other reports suggest that it is challenging to realize reversible O redox with 3*d* TM-based NIB materials.[15,25–27] Furthermore, oxygen gas release through mass spectrometry detects only the irreversible oxygen evolution,[5,13,19,28] and the true relationship between oxygen release and lattice O redox remains unclarified.[28,29] Therefore, a direct and reliable quantification of the oxygen chemistry in the bulk lattice over extended electrochemical cycles is critical for truly assessing the reversibility of lattice O redox in TM oxide cathodes.

Technically, a direct and reliable detection of the intrinsic O redox is a non-trivial issue. A quantitative probe of the lattice oxygen with truly elemental (oxygen) and chemical (state) sensitivity is required. While popular soft X-ray O-*K* studies of XPS and XAS have inspired important debates on O redox,[2–6,13] they suffer technical limitations from their probe depths (6.3 nm with 1.487 keV, 29 nm with 6.9 keV source for XPS[12]) and overwhelming effect from TM-O hybridization in XAS, as briefly explained above.[20] With such concerns and the need for a reliable characterization of lattice O redox, we have recently developed ultra-high-efficiency soft X-ray full-range mapping of resonant inelastic X-ray scattering (mRIXS),[30] which was soon demonstrated to be a sensitive and a reliable probe of the TM and O redox in bulk battery electrodes beyond conventional XAS.[31–33] Compared with XAS, mRIXS further resolves the energy of the fluorescence photon, called emission energy, which is completely missing in XAS.[20] In particular, a specific O-*K* mRIXS feature at 523.7 eV emission energy, different from that of TM-O hybridization feature at 525 eV, emerges only from the high-voltage charge plateau in Li-rich compounds,[31] and only in O-redox systems.[33] This feature is buried in conventional XAS

[1]School of Metallurgy, Northeastern University, Shenyang 110819, China

[2]Advanced Light Source, Lawrence Berkeley National Laboratory, Berkeley, CA 94720, USA

[3]Energy Storage and Distributed Resources Division, Energy Technologies Area, Lawrence Berkeley National Laboratory, Berkeley, CA 94720, USA

[4]Geballe Laboratory for Advanced Materials, Stanford University, Stanford, CA 94305, USA

[5]School of Advanced Materials, Peking University Shenzhen Graduate School, Shenzhen 518055, China

[6]School of Physics, National Key Laboratory of Crystal Materials, Shandong University, Jinan 250100, China

[7]Department of Materials Science and Engineering, Binghamton University, Binghamton, NY 13902, USA

[8]School of Materials Science and Engineering, Zhengzhou University, Zhengzhou 450001, China

[9]College of Physics and Materials Science, Tianjin Normal University, Tianjin 300387, China

[10]Department of Chemistry, Stanford University, Stanford, CA 94305, USA

[11]Department of Materials Science & Engineering, Stanford University, Stanford, CA 94305, USA

[12]Stanford Institute for Materials and Energy Sciences, SLAC National Accelerator Laboratory, Menlo Park, CA 94025, USA

[13]Department of Electrical Engineering, Tsinghua University, Beijing 100084, China

[14]Lead Contact

*Correspondence: gliu@lbl.gov (G.L.), wlyang@lbl.gov (W.Y.)

https://doi.org/10.1016/j.joule.2018.11.014

lineshape,[31,33] but manifests itself in the scanning transmission X-ray microscopy (STXM) only when the probe is moved away from the surface for tens of nanometers.[31] It is important to note that although the probe depth is the same (100 nm) for both XAS in fluorescence mode and for mRIXS, mRIXS does not suffer the lineshape distortion as in fluorescence XAS, and the bulk sensitivity of mRIXS for probing O redox is further enhanced by resolving emission energies, i.e., bulk and surface signals fortunately display different emission energies in mRIXS. For example, comparison with STXM of Li-rich materials directly show that signals corresponding to the mRIXS O-redox feature only show up when the probe is moved deeper than tens of nanometers, i.e., the 523.7-eV emission-energy mRIXS signal fingerprints lattice O redox not only due to the probe depth, but also through the specific emission-energy values.[31] While STXM provides important proof of the bulk sensitivity of mRIXS through emission energies, it requires transmission electron microscopy-type nanoparticle samples, and mRIXS provides the important advantage of being able to measure all electrodes in any forms.

Furthermore, recent combined studies of mRIXS experiments and theoretical calculations based on the OCEAN package of Li_2O_2 show that the mRIXS feature at 523.7 eV emission energy stems from a specific O 2*p*-2*p* intra-band exciton.[34] Such excitations require a partially unoccupied O-2*p* orbital (so electrons could be excited to the unoccupied 2*p* states), which naturally fingerprints the oxidized oxygen states because O^{2-} has no unoccupied 2*p* state. Although the specific excitations in the more complex TM systems are yet to be revealed by further works, these experimental and theoretical studies demonstrate that the specific mRIXS feature is a reliable fingerprint of the oxidized oxygen state with enough elemental and chemical sensitivity to differentiate the lattice O-redox signals in battery electrodes from the dominating hybridization features.[20] It is also important to note that mRIXS images reveal the full profile of O-redox features along both the excitation and emission energies. Such a full profile is particularly important for a reliable quantification because different systems of oxidized oxygen may display different profiles, e.g., Li_2O_2 shows a long profile along excitation energies, which cannot be detected through individual cuts in conventional RIXS experiments.[5,13,19] Therefore, these mRIXS developments and observations have now set a solid foundation for quantitative analysis of the lattice O redox in batteries.

On the other hand, almost all the O-redox active electrodes involve cationic redox reactions, simultaneously or separately.[35,36] As directly shown later in this work, even for a system with nominally pure O redox, TM redox will emerge with electrochemical cycling and affects the O redox. Direct probes of TM redox, together with O redox, will provide a consistent and experimental clarification of the reaction mechanism responsible for the total capacity, as well as the critical relationship between the anionic and cationic redox. The TM redox has more often been measured by hard X-ray XAS of the *K*-edges, through the edge shifting of the 2*s*-4*p* excitation features.[37] However, for 3*d* TMs, soft X-ray TM-*L* edges correspond to the excitations from 2*p* to directly the valence 3*d* states, providing a more direct probe of the TM 3*d* states,[37,38] which is more sensitive to valence electron states and could be easily quantified.[39,40] Unfortunately, the bulk-probe mode, namely fluorescence yield (FY), of the TM-*L* XAS, is known to be distorted due to the self-absorption effect,[41] leading to complicated situations that require theoretical calculations for quantitative analysis.[42] In 2011, Achkar et al. demonstrated soft X-ray inverse partial fluorescence yield (iPFY) as a non-distorted bulk probe of TM-3*d* states.[41] Such a technique has now been much improved through the 0.2- to 0.4-eV energy resolution of mRIXS, which enables the iPFY technique for all TM elements involved in

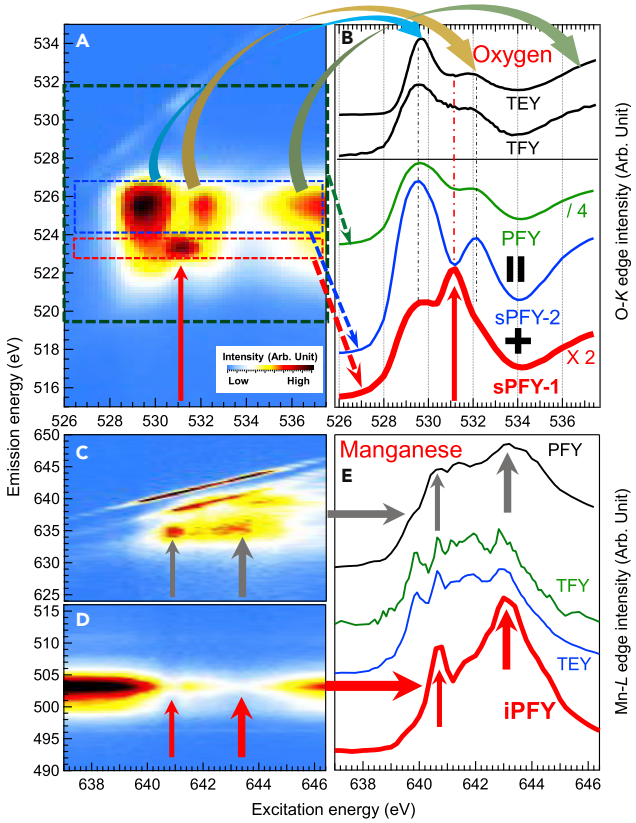

Figure 1. mRIXS of O-*K*/Mn-*L* and Their sPFY/iPFY Analysis for a Direct Probe of Bulk Redox

(A and B) O-*K* mRIXS of a typical $Na_{2/3}Mg_{1/3}Mn_{2/3}O_2$ NIB electrode at charged state (A). sPFY spectra (red) plotted in (B) are extracted by vertically integrating the signal across a super-partial range marked by the red (sPFY-1) and blue (sPFY-2) frames in (A). Conventional O-*K* PFY (green frame), TFY, and TEY data of XAS are plotted in (B) for comparison. mRIXS-sPFY selectively integrates the mRIXS features in a specific emission-energy region, so the sPFY peak area provides the opportunity for quantifying the mRIXS features of interest in both excitation and emission-energy dimensions, something that cannot be achieved through individual cuts in conventional RIXS.

(C–E) Are mRIXS images with excitation energy at the same Mn-*L* edge range (C and D), but with emission energy at (C) Mn-*L* and (D) O-*K*-edges. The diagonal features in the top left part of (A) and (C) are elastic features used for energy calibration. Integration of the intensity in (C) leads to the Mn-*L* PFY spectrum in (E). The inverse of the integrated intensity of (D) is the Mn-*L* iPFY, which is a non-distorted FY bulk probe of the Mn-3*d* valence states. Conventional TFY and TEY data of Mn-*L* XAS are plotted in (E) for comparison.

practical battery cathodes, especially Mn.[30] Obtaining non-distorted bulk TM-*L* spectra through mRIXS opens up the opportunity of a straightforward quantification of the bulk TM redox based directly on the TM-3*d* state measurements.

In this work, we further developed the mRIXS technique and demonstrate direct and reliable quantifications of the evolution of both the oxygen and TM redox states upon hundreds of cycles in two contrasting electrode systems. As shown in Figure 1 and elaborated later, by extracting the super-partial fluorescence yield (sPFY) within the characteristic emission-energy range of O redox in O-*K* mRIXS, the variation of lattice O-redox states could be quantified at different stages and at different cycles of electrochemical cycles. In the meantime, the extracted iPFY data from TM-*L* mRIXS allow quantitative definition of the bulk TM oxidation states based on the established linear-fitting method.[39] The combination of the final analysis of O-*K*

mRIXS-sPFY and Mn-*L* mRIXS-iPFY provides a complete picture of the evolution of both the anionic and cationic redox in $Na_{2/3}Mg_{1/3}Mn_{2/3}O_2$ at different potentials and for 100 cycles.

The material we focused on in this study is $Na_{2/3}Mg_{1/3}Mn_{2/3}O_2$, with its stoichiometry deliberately adjusted based on the $Na_{2/3}[Mg_{0.28}Mn_{0.72}]O_2$ electrodes previously reported by Yabuuchi et al.[43] Our adjusted stoichiometry increases the nominal valence of Mn to 4+, i.e., $1_{Na} \times 2/3 + 2_{Mg} \times 1/3 + 4_{Mn} \times 2/3 = 2_O \times 2$ to minimize the Mn redox during the initial charge process. Compared with the previous report,[43] our material displays an even higher initial charge capacity (162 mAh g^{-1}) and a much larger contribution from the high-voltage charge plateau. We note that because cathode is the source of Na ions in common NIBs, the initial charge capacity of the cathode is practically important for NIB full cells. Considering the high valence of Mn in the pristine material and the high initial charge capacity, this redesigned stoichiometry of $Na_{2/3}Mg_{1/3}Mn_{2/3}O_2$ makes the material a perfect candidate to study the evolution (reversibility) of O redox. In addition, we employed the mRIXS-sPFY analysis to a typical Li-rich compound, $Li_{1.17}Ni_{0.21}Co_{0.08}Mn_{0.54}O_2$, as reported previously,[31] which successfully reveals the reversibility and cyclability of the lattice O-redox activities in a Li-rich electrode with known gas release and surface reactions involved.

Our final results of both the oxygen and TM redox quantifications are self-consistent and decipher the total capacity of $Na_{2/3}Mg_{1/3}Mn_{2/3}O_2$. The data show that O redox is 79% reversible during the initial charge/discharge cycle and remains stable for up to 50 cycles. After 50 cycles, 87% capacity is sustained at the 100^{th} cycle. The quantifications also show that cationic (Mn) redox in $Na_{2/3}Mg_{1/3}Mn_{2/3}O_2$ emerges during the first discharge and develops low-valence Mn^{2+} on the surface. Recent observations show that TM valence states continuously drop upon cycling redox in Li-rich electrodes, contributing to voltage fade.[44] Here, evolution toward low-valence Mn in bulk is small, but the increase of low-valence Mn, especially Mn^{2+}, is clearly observed on the electrode surface, which is largely responsible for the voltage fade. Furthermore, the same mRIXS-sPFY analysis reveals a surprisingly high initial-cycle reversibility of the lattice (bulk) O-redox reaction in $Li_{1.17}Ni_{0.21}Co_{0.08}Mn_{0.54}O_2$ (76%), considering the system is known to involve serious gas release and surface reactions, but with only 44% capacity retention after 500 cycles. Our results demonstrate direct (Mn-3*d*, O-2*p*) and reliable experimental quantification of the changing cationic and anionic redox states in bulk lattice, and indicate that NIB and LIB materials share the same fundamental mechanism of O redox. The lattice O redox displays high reversibility, but capacity decay is obvious in systems involving other non-lattice oxygen activities. The contrast between the two different systems indicates that our conventional understanding of O redox was confused by mixing lattice O redox with oxygen release and/or surface reactions. While other redox-active oxygen activities are irreversible, lattice O redox could be highly reversible for hundreds of cycles in both NIBs and LIBs.

RESULTS AND DISCUSSION

mRIXS, sPFY of O-*K*, and iPFY of Mn-*L*

For a better readability and technical validity, we first explain our technical approaches for direct probes of the O-2*p* and TM-3*d* valence states through O-*K* and Mn-*L* mRIXS, respectively. We also explain the sPFY and iPFY analysis of the mRIXS results for the quantifications of the oxygen and TM states. Although iPFY

itself and its advantages over conventional XAS has been introduced before,[41] iPFY through mRIXS provides much more information on the relevant spectroscopic excitations due to its greatly improved resolution compared with previous reports.[20] It is important to note that, although sPFY is plotted upon the same excitation axis of XAS for comparison purposes, features of sPFY are fundamentally different from XAS features as they are associated with a very narrow (super-partial) emission-energy range, i.e., mRIXS-sPFY is plotted in the way of XAS for readability purposes, but sPFY features are of RIXS character, not XAS.

Figure 1A shows a typical O-*K* mRIXS result collected on a charged electrode (sample detailed below), with its sPFY analysis in Figure 1B. mRIXS shows the intensity (in color scale) distribution upon both the excitation (horizontal axis, same as the energies in XAS) and emission energies (vertical axis, missing in XAS).[20] The sum of all the fluorescence counts along the vertical axis is what conventional XAS collects in total fluorescence yield (TFY) mode. Integrating within the main O-*K* signal range (519–529 eV emission energy) gives the typical partial fluorescence yield (PFY). Consistent with all previous publications, the XAS in PFY, TFY, and TEY (total electron yield) (Figure 1B) consists of three main features corresponding to the three intensity packets of fluorescence signals in mRIXS around 525 eV emission energy (top arrows in Figure 1). Although large-energy-scale mRIXS has only been realized recently,[30] these three broad features along 525 eV emission energy have been identified as features from the O-2*p* bands (>534 eV excitation energy) and its hybridizations to TMs (529 and 532 eV excitation energies) through conventional RIXS cuts, as previously reviewed in fundamental physics.[45] Such an assignment could also be directly seen in Figure 1B, because their excitation energies match exactly the conventional XAS features with the same assignment, i.e., features in conventional XAS are dominated by only the 525 eV emission-energy features from standard oxygen (O^{2-}) signals.

Consistent with the O-redox feature identified in LIB systems,[20,31,33] mRIXS clearly shows a sharp feature at 523.7 eV emission energy (red arrows in Figures 1A and 1B). RIXS features at 523.7 emission energy have been found in oxidized oxygen systems, e.g., O_2 gas and peroxides.[34,46] The excitation energy of this feature, 531 eV, is within the energy range of those of non-divalent oxygen species, but is much sharper compared with peroxides and is material dependent.[34] Therefore, this O-*K* mRIXS feature at 523.7 eV emission energy and 531 eV excitation energy provides a reliable spectroscopic fingerprint of the non-divalent oxygen, i.e., oxidized oxygen, in battery electrodes at charged states.

By integrating the intensity across the narrow emission-energy range around the characteristic emission energies of 523.7 eV (red frame in Figure 1A) and 525 eV (blue frame in Figure 1A), a super-partial fluorescence yield (sPFY) signal quantifies the intensity of the specific mRIXS features from specific origins. As shown at the bottom of Figure 1B, the sPFY-1 of the 523.7 eV emission-energy range (red) displays a distinct peak at 531 eV excitation energy, which represents the O-redox activities. However, all conventional XAS lineshapes are dominated by the broad and strong features around 525 eV emission energy, as shown by sPFY-2 (blue frame). As explained above, RIXS features at 525 eV emission are of standard O^{2-} character from both broad O-2*p* bands and TM-O hybridization.[45] Therefore, O-*K* mRIXS successfully distinguishes the lattice O-redox signals from other strong contributions. More importantly, through a full energy-range map along both emission energy and excitation energies in mRIXS, sPFY around 523.7 eV emission energy (red frame in Figure 1A) contains the full-range mRIXS intensity along emission

energy, which enables a quantification of the total O-redox signals if the sPFY is further integrated along excitation energies, as demonstrated below.

A technical note is that X-ray radiation may affect the oxidized oxygen species,[47] which may decrease the O-redox signals. Careful radiation dose tests found that $Na_{2/3}Mg_{1/3}Mn_{2/3}O_2$ is stable across a large X-ray dose range, but Li-rich compounds display some decrease of the O-redox feature intensity upon high X-ray dose, which will be reported separately. Although we have carefully controlled the radiation dose with a relatively relaxed beam size of 20–30 μm for mRIXS experiments, there is still a possibility that the O-redox intensity of $Li_{1.17}Ni_{0.21}Co_{0.08}Mn_{0.54}O_2$ is underestimated in experiments due to the irradiation effect. However, as elaborated later, the majority of the contrast between the two systems is undoubtedly dominated by the intrinsic differences of the redox-active oxygen behaviors, e.g., whether the system involves oxygen release and surface reactions, and whether the O and TM redox are missed.

For a demonstration of the direct probe of TM-3*d* states through mRIXS, Figures 1C–1E show the contrast between the Mn-*L* mRIXS-iPFY analysis and conventional XAS. The principle of iPFY has been explained before,[41] and demonstrations of Mn-*L* iPFY analysis of mRIXS were also realized in our high-efficiency mRIXS system.[30] In brief, with the excitation energy range covering Mn-*L* edges, e.g., 638–646 eV for Mn-L_3 edge, the incident X-rays also excite O-*K* features at emission-energy range of 495–510 eV (Figure 1D). The intensity of such a non-resonant O-*K* emission is affected by the absorption coefficient of the incident photons at the Mn-*L* energy range, leading to (inversed) dips corresponding to the intrinsic Mn-*L* absorption peaks.[30] Therefore, through the high energy resolution of the mRIXS results, a $PFY_{O\text{-}K}$ can be obtained by integrating the mRIXS intensity within the O-*K* emission range (495–510 eV, Figure 1D), and its inverse value iPFY = $1/PFY_{O\text{-}K}$ provides a bulk-sensitive (photon-in-photon-out) probe of the intrinsic Mn-*L* absorption coefficient without any spectral distortion. The Mn-*L* iPFY spectrum in Figure 1E (red) displays an exact Mn^{4+} spectrum in the charged electrodes,[48] contrasting the spectra from other conventional XAS channels, including TEY, TFY, and PFY. Such Mn-*L* data in the bulk-probe (probe depth of about 200 nm in Mn-*L* edges) fluorescence mode naturally enables the quantitative fittings of the bulk TM oxidation states, which have been established for various TM-*L* edges.[39] In addition, although mRIXS-iPFY still contains surface signals, when compared with the surface-sensitive (10 nm probe depth) TEY spectra, such a non-distorted detection with >100 nm probe depth provides direct contrast between the bulk and surface chemistry of the electrodes. In the following paragraphs all Mn-*L* raw data were collected through full-range mRIXS, but for clarity we focus on the final iPFY results and their comparison with the TEY surface signals.

Materials and Electrochemical Properties

The $Na_{2/3}Mg_{1/3}Mn_{2/3}O_2$ material is synthesized by a poly(vinyl pyrrolidone) (PVP)-assisted gel combustion method.[49,50] This stoichiometry is adjusted so that the nominal valence of Mn in the material is pure +4, i.e., Mn redox is intentionally suppressed during the initial charge. Structural characterizations through X-ray powder diffraction (XRD) and scanning electron microscopy (SEM) are presented in Figures S1 and S2. The XRD (Figure S1) shows the same pattern as $Na_{2/3}[Mg_{0.28}Mn_{0.72}]O_2$.[43] All diffraction peaks can be indexed as a hexagonal structure with a $P6_3/mmc$ space group, i.e., P2-type. The peak at 20.6° is due to the formation of $\sqrt{3}a \times \sqrt{3}a$-type in-plane superlattice between Mg^{2+} and Mn^{4+}.[51] Figure S2 shows the SEM image of the well-crystallized morphology of $Na_{2/3}Mg_{1/3}Mn_{2/3}O_2$ as well as calculated particle size distribution.

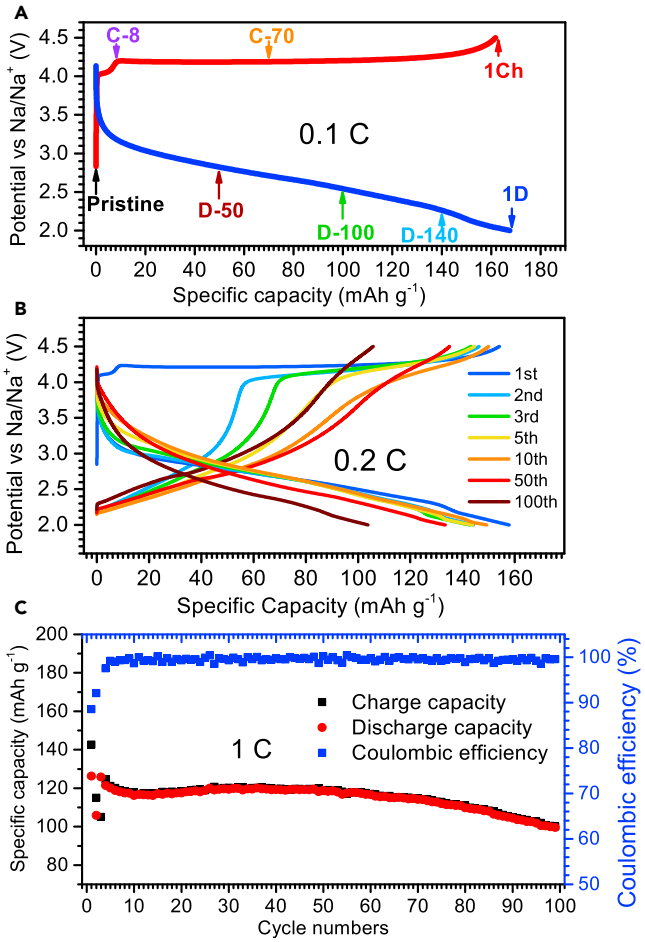

Figure 2. Electrochemical Properties of $Na_{2/3}Mg_{1/3}Mn_{2/3}O_2$

(A) The initial charge and discharge profiles of the $Na_{2/3}Mg_{1/3}Mn_{2/3}O_2$ at 0.1 C. The points tested by XAS and RIXS are marked with arrows.

(B) The electrochemical profiles of different cycles at 0.2 C.

(C) Capacity retention and Coulomb efficiency with 1 C cycling rate.

See also Figures S3–S7.

The particle size is between 0.5 and 3 μm. The particles are smooth-faced without secondary particle structure. Such morphology is generally desirable for improving the electrochemical performance.

The electrochemical performance of $Na_{2/3}Mg_{1/3}Mn_{2/3}O_2$ electrodes is shown in Figure 2. A short plateau of only 8 mAh g^{-1} capacity appears at 4.0 V before the potential reaches a very long 4.2 V (open-circuit voltage is ~4.1 V, Figure S3B) plateau, corresponding to a strong peak at 4.3 V in the cyclic voltammetry curves shown in Figure S3A. The overall initial charge capacity reaches 162 mAh g^{-1}, which is dominated by the 4.2-V plateau. Note again that this improved initial charge capacity is practically important for NIBs. This also means that the Na^+ can be extracted near 0.56 mol and the formula of charged electrode is $Na_{0.11}Mg_{1/3}Mn_{2/3}O_2$. Although this work does not focus on the material itself, we note that this is the highest initial charge capacity value reported for air-stable P2-type sodium TM oxides. The good rate capability is shown in Figure S4. Compared with the initial study of $Na_{2/3}[Mg_{0.28}Mn_{0.72}]O_2$ electrode with 150 mAh g^{-1} charge capacity,[43] the capacity

before the 4.2 V charge plateau decreases due to the further suppression of the Mn redox in $Na_{2/3}Mg_{1/3}Mn_{2/3}O_2$. Note that the suppression of the cation TM redox leads to a counterintuitive increase of the initial charge capacity through the long 4.2-V charge plateau. This indirectly indicates the highly active oxygen in the $Na_{2/3}Mg_{1/3}Mn_{2/3}O_2$ electrode during electrochemical operations, providing an optimized candidate for O-redox studies.

Figures 2B and S5 compare the charge and discharge profiles at 1st, 2nd, 3rd, 5th, 10th, 50th, and 100th cycles. Cycling profiles with other potential range were measured and plotted in Figure S6. The cycling profile clearly shows that the capacity of the 4.2-V plateau drops continuously with electrochemical cycles. Figure 2C shows the charge and discharge capacity retention and the Coulombic efficiency at 1 C. The capacity retention is 80% after 100 cycles. The average Coulombic efficiency during cycling is 99.3% excluding some abnormal points. The long-term cycling performance for 2.0–4.5 V and 1.5–4.5 V at 1 C and 2.0–4.5 V at 0.2 C are shown in Figure S7. The high-voltage plateau is often used as an indicator of O redox. If such an assumption were valid, the cycling profile implies that O redox is only partially reversible for about ten cycles before it disappears in this system. It is therefore critical to experimentally clarify the activity of O redox beyond ten cycles.

Mn States in Bulk and on Surface upon Electrochemical Cycling

We first clarify the Mn-redox activities of $Na_{2/3}Mg_{1/3}Mn_{2/3}O_2$ electrodes in the bulk and on the surface upon electrochemical cycling. As explained above, Mn-3*d* valence states in the bulk are measured through the Mn-*L* mRIXS-iPFY spectra. Surface signals are collected through conventional XAS-TEY.[38] Because both datasets represent intrinsic absorption coefficient without lineshape distortion, they could be reliably quantified based on a simple linear combination of the distinct lineshape of $Mn^{2+/3+/4+}$ references,[48,52] which has been successfully demonstrated for obtaining quantitative contrast of the bulk and surface Mn states.[39,53]

Mn-L_3 iPFY and TEY spectra are overplotted for direct comparison of the bulk and surface Mn states. Spectra with different potentials during the initial cycle are plotted in Figure 3, and data with extended cycles are displayed in Figure 4. For the important bulk signal associated with the lattice O redox discussed later, quantitative fittings of iPFY are plotted directly in the figures (dotted line) to show the satisfactory simulation. The full energy-range TEY spectra of more samples and their quantitative fitting plots are shown in Figures S8 and S9. The conventional TFY spectra are also plotted in Figures S10 and S11 for reference. Fittings of both iPFY and TEY results highly agree with experimental data, providing a reliable determination of the Mn oxidation states in bulk and on surface. The contrast between the iPFY and TEY spectra clearly shows the emergence of a surface inactive layer of Mn^{2+} upon cycling, indicated by the 640-eV peak only found in TEY data. Such a contrast, as well as the overall bulk redox evolution upon cycling, is visualized in the fitting results plotted in Figures 3B and 4B. The values of Mn valence percentages by fitting iPFY (bulk) and TEY (surface) spectra are shown in Table 1.

For the initial charge and discharge cycle (Figure 3), a trace amount of about 5% Mn^{3+} is found in the pristine material, which is fully oxidized to Mn^{4+} during the very short 8 mAh g^{-1} charging process (C-8), corresponding to the small charge capacity at 4.0 V in Figure 2A. The Mn^{4+} state then remains unchanged until the potential drops below 2.5 V during discharge. It is clear that the adjusted stoichiometry of $Na_{2/3}Mg_{1/3}Mn_{2/3}O_2$ indeed suppresses the Mn redox during the initial charge process, and Mn in bulk remains at Mn^{4+} throughout the large-capacity 4.2-V charge

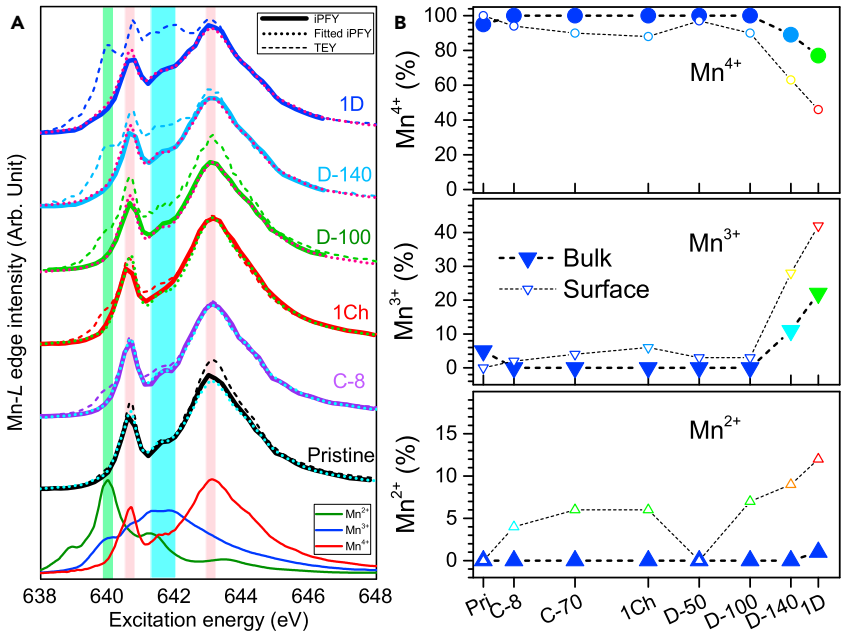

Figure 3. Mn-L_3 iPFY and TEY Spectra and the Quantified Bulk and Surface Mn Valence States of $Na_{2/3}Mg_{1/3}Mn_{2/3}O_2$ Electrodes at Representative SoC Levels during the Initial Cycle Indicated in Figure 2A

(A) The Mn-L_3 edge iPFY (solid line), fitted iPFY (dotted line), and TEY (dashed line) spectra. References of MnO (Mn^{2+}), Mn_2O_3 (Mn^{3+}), and Li_2MnO_3 (Mn^{4+}) are plotted at the bottom for direct comparison.

(B) The fitting results of the Mn valence distributions in bulk (solid points) and on surface (hollow points) at different electrochemical stages. Error bars for fitted bulk Mn states are smaller than the symbols and are therefore not shown.

See also Figures S8 and S10.

plateau. However, Mn^{3+} starts to develop at low potentials during discharge (D-100 to D-140). The D-140 and fully discharged (1D) electrode have about 11% and 23% Mn^{3+} with a trace contribution from Mn^{2+}, corresponding to 0.07 and 0.16 mol electron transfer per 1 mol $Na_{2/3}Mg_{1/3}Mn_{2/3}O_2$ due to Mn reduction, respectively.

In contrast, the Mn states on the surface show a very different trend. The surface Mn of the pristine electrode is fully Mn^{4+}, suggesting that Mn^{3+} does not appear on the surface of $Na_{2/3}Mg_{1/3}Mn_{2/3}O_2$ like the spinel $LiMn_2O_4$. However, during charging, the surface Mn^{2+} and Mn^{3+} are increasing, which is different from that of $Na_{0.44}MnO_2$ in which no O redox is involved.[53] At the initial stage of discharge, the surface Mn is oxidized slightly to +4 valence (D-50) and then gradually reduced during the discharge progress, resulting in a rapid increase of surface Mn^{2+}. Therefore, the surface activities in such an O-redox system are obviously affected by two different factors: some surface reactions that are likely associated with the oxidized oxygen during charge, and the surface reduction effect by the electrochemical discharge itself.

For the electrodes with extended cycles (Figure 4), the Mn^{2+} on the surface continuously increases with the cycle. The surface Mn^{2+} content reaches 35% after 100 cycles, which could be seen directly through the TEY spectra of both charged and discharged electrodes. This indicates that only part of the surface Mn^{2+} is electrochemically active. On the other hand, the iPFY analysis of the Mn states in the bulk shows that $Mn^{3+/4+}$ redox remains stable over 100 cycles, despite of the obvious

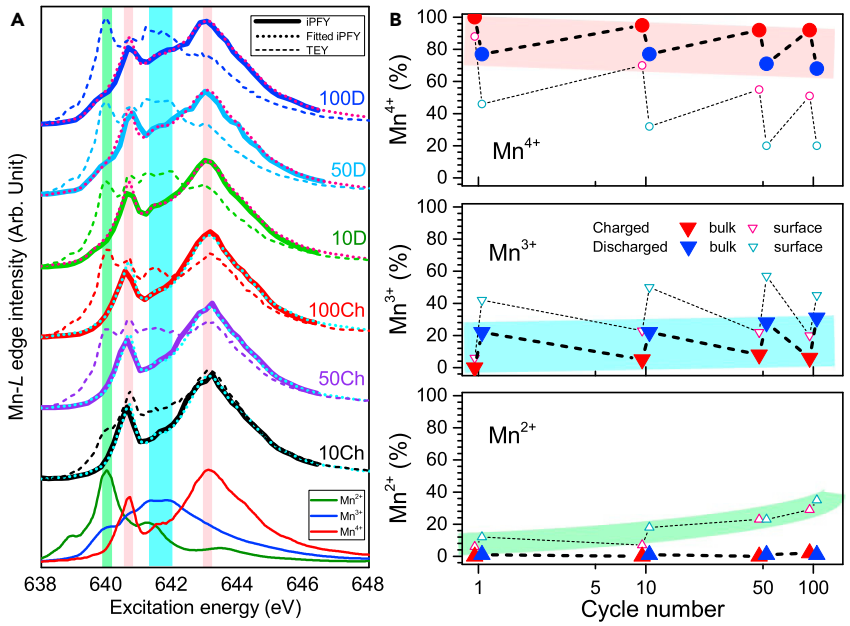

Figure 4. Mn-L_3 Edge Spectra and the Calculated Bulk and Surface Mn Valence States of Charged and Discharged $Na_{2/3}Mg_{1/3}Mn_{2/3}O_2$ Electrodes after Different Cycles

(A) The Mn-L_3 edge iPFY (solid line), fitted iPFY (dotted line), and TEY (dashed line) spectra of $Na_{2/3}Mg_{1/3}Mn_{2/3}O_2$ electrodes. References of MnO (Mn^{2+}), Mn_2O_3 (Mn^{3+}), and Li_2MnO_3 (Mn^{4+}) are plotted at the bottom for direct comparison.

(B) The fitting results of the Mn valence distributions in bulk (big solid points) and on surface (small hollow points) at different cycles. Error bars for fitted bulk Mn states are smaller than the symbols and are therefore not shown.

See also Figures S9 and S11.

change of the electrochemical profile (Figure 2B). Although the $Mn^{3+/4+}$ redox is stable upon cycling, the amount of Mn^{3+} displays very slow increment upon cycling. We note that the TM valence drop in the bulk has recently been reported in Li-rich materials to explain the voltage fade therein.[44] Mn-*L* edge provides a more direct quantification of the 3*d* valence states in the bulk and on the surface, and the results here indicate that voltage fade in $Na_{2/3}Mg_{1/3}Mn_{2/3}O_2$ could also be from the decreasing Mn valence upon cycling, especially on the electrode surface. Of course, the voltage fade here is smaller than that in typical Li-rich compounds.[44] Future detailed and comparative studies on voltage fade based on the same type of materials are critical to further clarify the origin of voltage decay and its association with redox activities.

Quantifying the Oxygen-Redox Reversibility during Initial Cycles

While the Mn-*L* iPFY suggests that majority of the capacity of $Na_{2/3}Mg_{1/3}Mn_{2/3}O_2$ electrodes is not from Mn redox, it only provides indirect evidence for O redox, especially with the clear evidence on strong surface reactions discussed above. Direct experimental evidence and quantifications of the oxygen state evolution upon extended cycles remain critical and are the key contributions of this work. The conventional O-*K* XAS (TEY and TFY) results of representative samples are shown in Figure S12. As discussed in the Introduction, XAS pre-edge lineshape changes do not represent the O redox in battery electrodes; instead, they represent the change on TM-O hybridization strength, and the changes upon electrochemical cycling could thus be observed in almost all battery electrodes, including spinel and olivine materials without O redox.[20,42,54] Therefore, features in the pre-edge range

Table 1. Mn Valence Percentage by Fitting from iPFY (Bulk) and TEY (Surface) Spectra

Sample	Bulk			Surface		
	Mn^{2+}	Mn^{3+}	Mn^{4+}	Mn^{2+}	Mn^{3+}	Mn^{4+}
Pri	0	5	95	0	0	100
C-8	0	0	100	4	2	94
C-70	–	–	–	6	4	90
1Ch	0	0	100	6	6	88
D-50	–	–	–	0	3	97
D-100	0	0	100	7	3	90
D-140	0	11	89	9	28	63
1D	1	22	77	12	42	46
10Ch	0	5	95	7	23	70
50Ch	0	8	92	23	22	55
100Ch	2	6	92	29	20	51
10D	1	22	77	18	50	32
50D	1	28	71	23	57	20
100D	1	31	68	35	45	20

The error is below ±3 percentage estimated from the uncertainty in the fitting procedure.

528–534 eV need to be further resolved to extract the reliable signals of O-redox states for quantifications.

Further resolving the XAS features in the 528–534 eV range is exactly what mRIXS measures.[20] Figure 5A show the O-*K* mRIXS of a series of electrodes, again denoted in Figure 2A, at different state of charge (SoC) during the initial charge and discharge. As specified above, the broad features around 525 eV emission energy (vertical axis) correspond to the O^{2-} states in typical TM oxides,[45] which can be seen in all samples. These features get broadened in lineshape and enhanced in intensity upon charging (oxidation) process, consistent with the many XAS observations but irrelevant to O-redox states. In contrast, the feature at 523.7 eV emission energy (red arrows) starts to emerge only when the potential reaches the 4.2-V plateau (Figure 2A, after C-8), and becomes strong at the charged state. During discharge, this feature is weakened gradually and disappears when the potential is below 2.5 V (after D-100).

Figure 5B is the sPFY of the 523.7-eV emission-energy feature extracted from mRIXS images, and the integrated area (the calculation is explained in Experimental Procedures) of the characteristic 531-eV sPFY peak is displayed in Figure 6 (hollow circles) together with the cycling profile. The 531-eV sPFY peak emerges after the 4.2-V charge plateau starts, reaches the maximum intensity at the fully charged state, and weakens until about 2.5 V in the discharge process.

Combining the area of the 531-eV O-*K* mRIXS-sPFY peak with the quantitative results of bulk Mn redox obtained through Mn-*L* mRIXS-iPFY (Figure 3), we now could explain the total capacity with the independent Mn- and O-redox quantifications (Figure 6). Overall, changes on Mn-*L* (Figure 3) and O-*K* (Figure 5) spectroscopic results take place at different electrochemical stages in the $Na_{2/3}Mg_{1/3}Mn_{2/3}O_2$ system. The O-*K* results show that oxygen oxidation starts at 4.2 V during initial charge, and stops at 2.5 V during the following discharge, within which Mn-*L* displays no change. This clearly defines the crossover points from oxygen to Mn-redox reactions

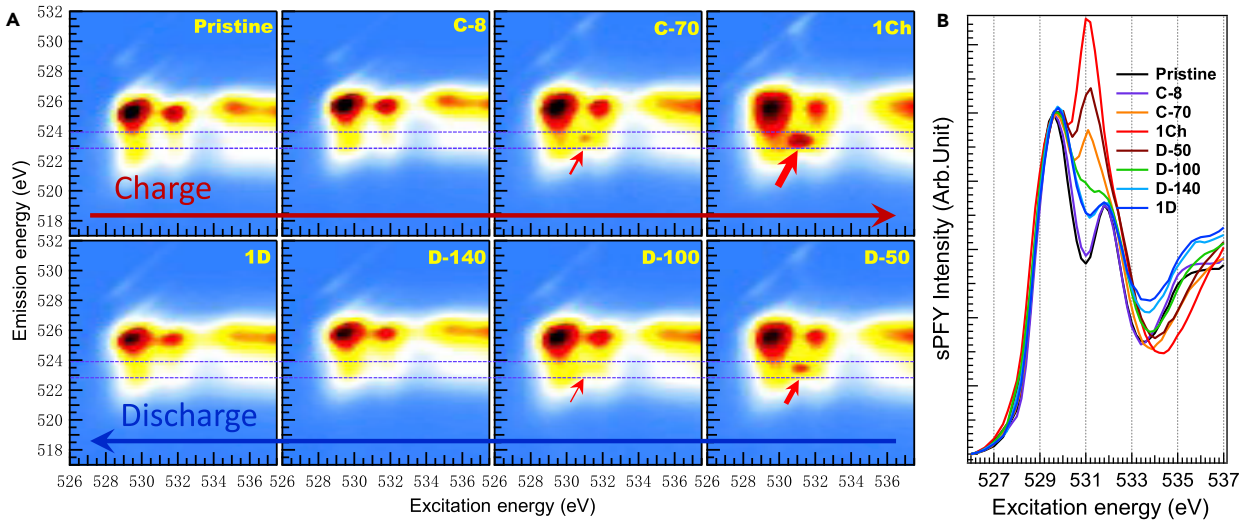

Figure 5. O-*K* mRIXS and sPFY during Initial Cycle

(A) The mRIXS images of $Na_{2/3}Mg_{1/3}Mn_{2/3}O_2$ electrodes at different SoC during initial cycle. Samples are marked in Figure 2A. The key O-redox feature that emerges at high potentials is indicated by the red arrows.

(B) sPFY spectra extracted from mRIXS by integrating the characteristic 523.7 eV emission-energy range, as indicated by the two horizontal purple dashed lines (see technical demonstrations of sPFY in Figure 1).

See also Figure S12.

at 4.2 V during charge and 2.5 V during discharge. Therefore, the corresponding charge compensation of Mn (blue in Figure 6A) and O (red in Figure 6A) redox are 0.03 mol and 0.53 mol during charging, and 0.16 mol and 0.42 mol during discharge, from electrochemical experiments (x axis of Figure 6).

These charge compensation numbers from the electrochemical measurements could now be determined by our Mn-*L* mRIXS-iPFY and O-*K* mRIXS-sPFY quantification values. First, for the main Mn-redox contribution during discharge, the quantified electron transfer number from Mn redox by calculations based on the Mn valences from mRIXS-iPFY results (Figure 3 and Table 1) is 0.16 mol at discharged state per 1 mol $Na_{2/3}Mg_{1/3}Mn_{2/3}O_2$ (rightmost column bar), matching exactly the electrochemical Na intercalation value during discharge (0.16 mol on bottom x axis). Second, for O-redox contributions, the O-*K* mRIXS-sPFY 531 eV peak intensity (open circles in Figure 6A) displays a changing ratio of 0.77/0.61 of the charge/discharge process, which matches exactly the electrochemical charge transfer of the O-redox regimes (0.53/0.42, bottom x axis of Figure 6A).

If we assume a linear dependence between the amount of O redox and O-*K* mRIXS-sPFY 531-eV peak area changes, the value of the spectroscopic peak area changes (left vertical axis of Figure 6B) are in great agreement with the electrochemical electron transfer numbers (x axis of Figure 6B). We note that, because the sPFY spectra were normalized to the hybridization feature for comparison purposes (see Experimental Procedures) and the hybridization feature is typically enhanced at charged state, the assumption of the linear dependence above should be modified for an absolute quantification of the amount of O redox at each electrochemical state (underestimated with linear dependence). However, in this work we focus on the variation of the sPFY peak area to address the reversibility of O redox, which only requires the same hybridization level at the same electrochemical state. The great agreement between sPFY analysis and

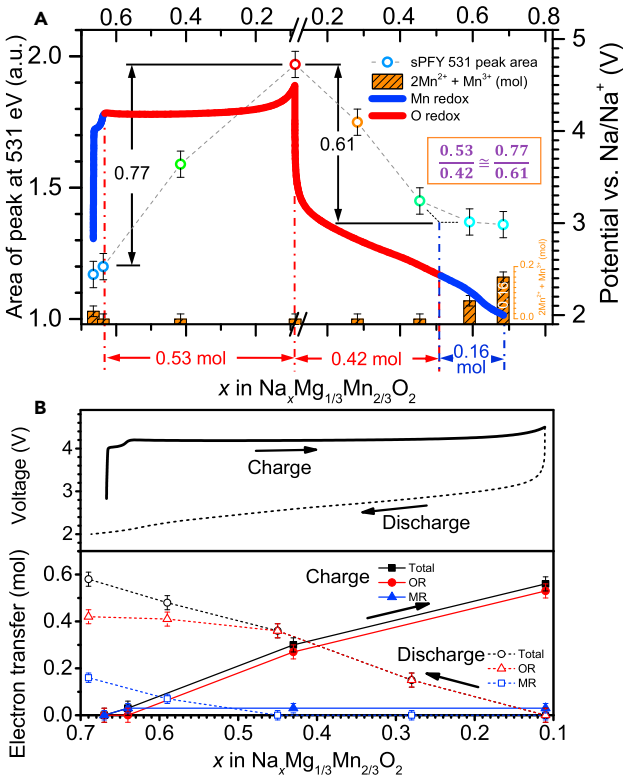

Figure 6. Deciphering the Total Electrochemical Capacity by Independent Quantifications of Mn-Redox and Changing O-Redox States

(A) The blue and red color of the electrochemical profile represent Mn-redox and O-redox regimes. The crossover points of 4.2 V during charge and 2.5 V during discharge are determined experimentally by whether the Mn and O spectroscopic signals change. In particular, the O-redox contributions are 0.53 mol and 0.42 mol during charge and discharge, respectively. Hollow circles are areas of O-*K* mRIXS-sPFY 531 eV peaks. The change of the peak area is 0.77 during charge and 0.61 during discharge. The ratio of the O-redox contributions during charge/discharge is consistently determined by either the electron transfer numbers (0.42/0.53) or mRIXS-sPFY peak area (0.61/0.77) as 79%. The Mn-redox contributions are quantified by the Mn valences from Mn-*L* mRIXS-iPFY results (column bars on the bottom). For example, the fully discharged state includes 0.16 mol electron transfer from Mn redox, which matches exactly the regime of Mn redox in electrochemical profile (0.16 mol).

(B) Accumulated electron transfer of Mn redox and O redox during charging and discharging. Again, Mn-redox contributions are calculated based on Mn valences from mRIXS-iPFY. O redox is calculated based on O-*K* mRIXS-sPFY peak area changes, assuming a linear dependence between the amount of O redox and the sPFY 531 eV peak area (see text on assumptions). Error bars are overestimated here considering all possible contributions from uncertainty in the fitting procedure, the resolving power of RIXS, and the upper and lower limits of scaling.

electrochemistry here suggests that this is a reasonable condition at least for $Na_{2/3}Mg_{1/3}Mn_{2/3}O_2$, whereby hybridization enhancement upon charge is likely minimized through mostly oxidized oxygen, instead of strong TM redox in other systems. Furthermore, our quantification here is based on a self-consistent analysis of both the spectroscopic variation and electrochemical profile. The independent quantification values of Mn- and O-redox reactions match and decipher the electrochemical capacity. The results from both sPFY peak area changes and electrochemical capacity (with range defined by mRIXS as explained above) reveal directly the reversibility rate of the lattice O redox during the initial cycle of $Na_{2/3}Mg_{1/3}Mn_{2/3}O_2$, i.e., 0.61/0.77 = 79%.

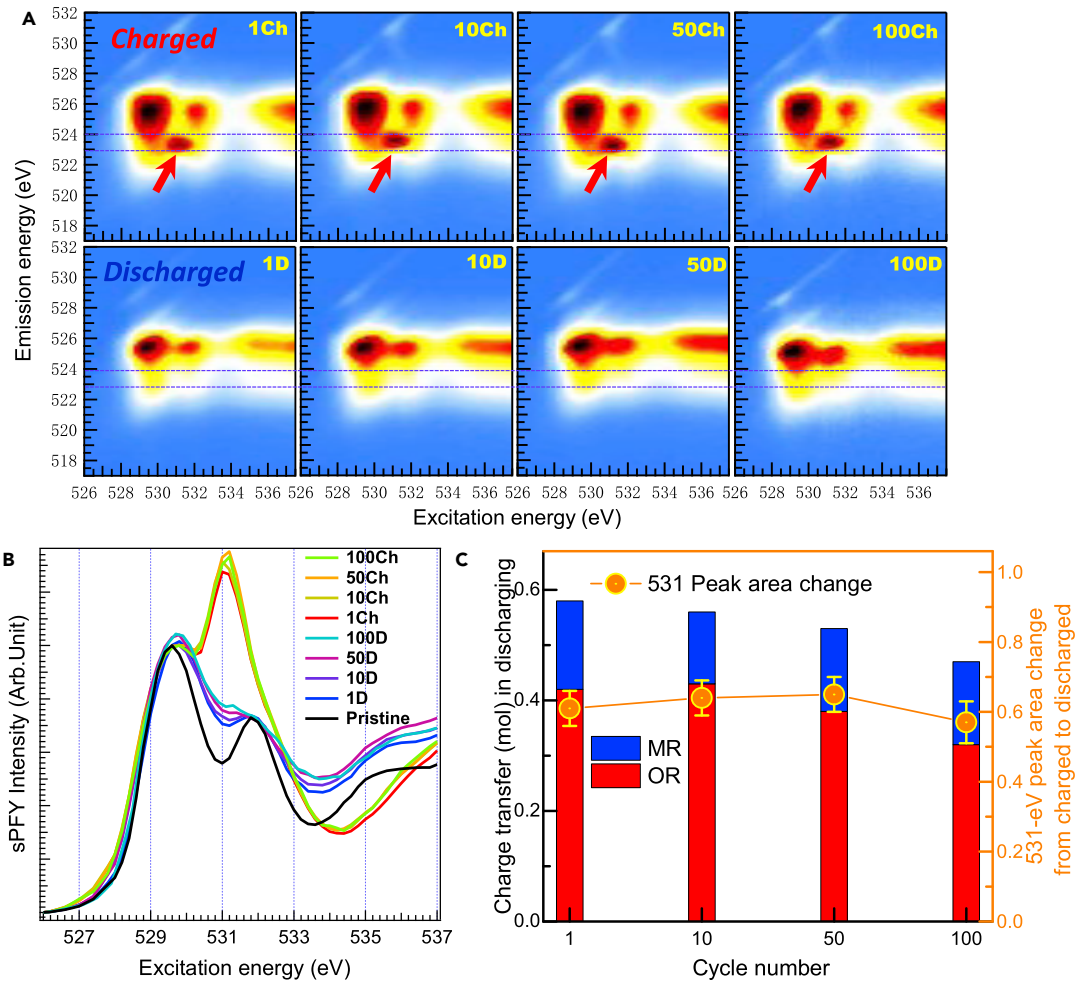

Figure 7. Cyclability of Oxygen and Mn Redox upon Cycling

(A) O-*K* mRIXS images of a series of charged (top) and discharged (bottom) electrode after the 1st, 10th, 50th, and 100th cycles. Red arrows indicate the oxidized oxygen features in charged states.

(B) sPFY spectra extracted from mRIXS by integrating the characteristic 523.7 eV emission-energy range (purple dashed lines). The oxidized oxygen peak remains strong and reversible over 100 cycles.

(C) The quantified electron transfer of Mn redox (blue bar), the expected value of O-redox contribution (red bar) calculated by subtracting Mn-redox contribution from total capacity, and the 531 O-*K* sPFY peak area changes between charged and discharged states at extended cycles. Error bars are overestimated here considering all possible contributions from uncertainty in the fitting procedure, the resolving power of RIXS, and the upper and lower limits of scaling.

See also Figure S12.

Cyclability of Oxygen Redox upon Extended Cycles

The characteristic O-redox feature in mRIXS and the quantitative peak area analysis through sPFY empower us to quantify the O-redox cyclability upon electrochemical cycling. This approach is employed to study electrodes with extended cycles, as shown in Figure 7. In general, the O-redox feature in mRIXS images displays amazing cyclability over 100 cycles of $Na_{2/3}Mg_{1/3}Mn_{2/3}O_2$ (Figure 7A), with a strong intensity at charged state (red arrows in top row) and disappearance at the discharged state (bottom row). Figure 7B shows that again the mRIXS-sPFY spectra are around 523.7 eV emission energy. The amounts of O redox at different cycles are quantified by the sPFY 531-eV peak intensity differences between the charged and discharged states at the 1st, 10th, 50th, and 100th cycles. The summary of the amount

Table 2. Charge-Transfer Numbers from Na^+, Mn Redox (MR), and O Redox (OR) upon Electrochemical Cycling

Cycle Number	n_{Na} in Discharge (mol)	Mn Average Valence		n_{MR} (mol)	n_{OR} (mol)
		Charged	Discharged		
1	0.58	4	3.76	0.16	0.42
10	0.56	3.95	3.76	0.13	0.44
50	0.53	3.92	3.70	0.15	0.45
100	0.47	3.90	3.67	0.15	0.39

The electron transfer number of MR, n_{MR}, is calculated by the Mn valence change from charged to discharged state (Figure 4 and Table 1) multiplied by 2/3 mol (2/3 mol Mn per 1 mol $Na_{2/3}Mg_{1/3}Mn_{2/3}O_2$). The electron transfer number of OR, n_{OR}, is calculated by the mRIXS-sPFY 531 eV peak area difference between charged and discharged state (Figures 7B and 7C), multiplied by the factor of (0.42/0.61) mol from the first discharge, as discussed in detail in Figure 6A.

of Mn redox, O redox, and the O-*K* mRIXS-sPFY 531 eV peak area change up to 100 cycles are displayed in Figure 7C and Table 2.

The quantitative analysis here shows that the O-redox activities are very stable up to 50 cycles, then start to decay with about 87% of the O redox sustained at the 100th cycle (Figure 7C and Table 2). We note that such quantification with extended cycles is impossible through the conventional XAS even technically, as shown in Figure S12, because the XAS spectra of charged and discharged electrodes become almost identical after only tens of cycles. An interesting phenomenon is that Figure 7B shows clearly that the 531 eV sPFY peak area at charged state does not decrease with cycling, whereas the overall intensity of the fully discharged states keeps increasing upon cycling. While such an increase is related to the overall peak broadening from structural amorphization upon cycling, i.e., lifting the dip between two peaks, the very systematic change at discharged states also implies that the decreasing of O-redox contents beyond 50 cycles may be associated with the deep discharging.

mRIXS Quantifications of the Lattice Oxygen Redox in $Li_{1.17}Ni_{0.21}Co_{0.08}Mn_{0.54}O_2$

In this section, we demonstrate that the mRIXS-sPFY analysis here could be employed for quantitative studies of lattice O redox in various battery electrodes, including those with oxygen gas evolution. It is important to emphasize that what mRIXS detects is the specific lattice O redox within the bulk electrodes, i.e., not the general/total O redox that includes other irreversible oxygen involvements. We also note that the lattice O redox is the critical part of the reactions that could be potentially useful for battery devices. The mRIXS technique, as a photon-in-photon-out bulk probe under vacuum environment, provides unique opportunities to focus on this practically meaningful lattice O-redox reaction, and to quantify its reversibility and cyclability.

For a comparative study, we employed the same O-*K* mRIXS-sPFY quantification to a more complex Li-rich compound, $Li_{1.17}Ni_{0.21}Co_{0.08}Mn_{0.54}O_2$. O redox in a Li-rich electrode system has been extensively studied recently.[5,12,13,28,31,33,44] We note that STXM results through non-distorted transmission mode could quantify the O redox during the initial cycle,[31] but samples for STXM need to be processed into individual nanoparticles due to the limited penetration depth of soft X-rays. In comparison, mRIXS could be directly employed on any form of electrodes with any size of particles and at any electrochemical states after extended cycles.

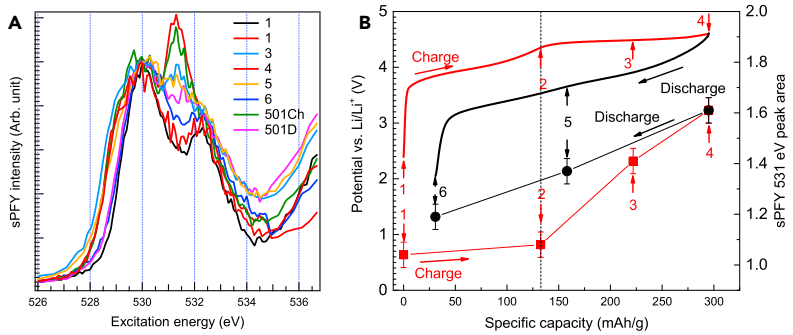

Figure 8. O-*K* mRIXS-sPFY Quantifications of Lattice Oxygen Redox in $Li_{1.17}Ni_{0.21}Co_{0.08}Mn_{0.54}O_2$

(A and B) The mRIXS-sPFY at 523.7 eV emission-energy range (see Figure 1A) of electrodes at different SoC during initial and extended cycle based on mRIXS results reported previously (A).[31] Samples during initial cycle are marked on the electrochemical profile in (B). Red squares in (B) are integrated area (right vertical axis) of the characteristic mRIXS-sPFY peak at 531 eV during charging (red arrows), which increases during the charge plateau but not below. Black dots represent the integrated O-redox peak area upon discharge (black arrows). Integrated peak area values after extended cycles are also analyzed and discussed in the text but are not shown in (B) for display clarity. Error bars are overestimated here considering all possible contributions from uncertainty in the fitting procedure, the resolving power of RIXS, and the upper and lower limits of scaling.

Figure 8A shows the mRIXS-sPFY results of a series of $Li_{1.17}Ni_{0.21}Co_{0.08}Mn_{0.54}O_2$ electrodes indicated on the electrochemical profile in Figure 8B, by integrating the same energy window as for our $Na_{2/3}Mg_{1/3}Mn_{2/3}O_2$ analysis (Figure 1A) of the mRIXS results reported previously.[31] Although a bit noisier than that of $Na_{2/3}Mg_{1/3}Mn_{2/3}O_2$, the 531-eV peak intensity displays clear variation at different electrochemical states. The peak area is plotted together with the electrochemical profile in Figure 8B (offset for display clarity). It is clear that the peak area remains unchanged before the 4.5 V charge plateau, but starts to increase during the charge plateau with roughly a linear dependence on charge capacity. In the following discharge, the area value decreases through most of the discharge process but does not recover to the pristine state. The change of the 531 eV peak area in the initial charging and discharging is 0.55 and 0.42, respectively; therefore, the reversibility of the O redox in the initial cycle is about 76%. After 500 cycles, the 531-eV peak area change from charge to discharged states is 0.24, suggesting a cyclability of 44%.

There are several important contrasts between the $Li_{1.17}Ni_{0.21}Co_{0.08}Mn_{0.54}O_2$ and $Na_{2/3}Mg_{1/3}Mn_{2/3}O_2$ systems indicated by our quantification results. First, there is a clear crossover point between the O- and Mn-redox reactions in $Na_{2/3}Mg_{1/3}Mn_{2/3}O_2$ (Figure 6A and discussions above); therefore, capacity contributions from O redox could be well defined during both charge and discharge processes that match the spectroscopic quantifications. However, for $Li_{1.17}Ni_{0.21}Co_{0.08}Mn_{0.54}O_2$, O-redox reactions take place throughout the discharge process mixed together with TM redox reactions.[31,44] Therefore, because of the contributions from TM redox, the electrochemical discharge capacity is much larger than that of the O-redox region during charge, i.e., the charge plateau. Nonetheless, mRIXS-sPFY is able to distinguish the lattice O-redox contributions from such a mixed redox process and reveals the 76% initial-cycle reversibility as elaborated above.

Second, another important contrast emerges if we further examine the quantification values of the O-redox contributions during the initial charge process. The electron transfer in the 4.5-V charging plateau for $Li_{1.17}Ni_{0.21}Co_{0.08}Mn_{0.54}O_2$ is 0.52 mol,

with a change in mRIXS-sPFY peak area of 0.55 (Figure 8B). $Na_{2/3}Mg_{1/3}Mn_{2/3}O_2$ displays 0.77 peak area change with 0.53 mol electron transfer (Figure 6A). Although the absolute value of the conversion ratio between the variation of mRIXS-sPFY peak area and electron transfer number could be highly material dependent due to the different hybridization background, the $Li_{1.17}Ni_{0.21}Co_{0.08}Mn_{0.54}O_2$ obviously displays much lower mRIXS variation than that in $Na_{2/3}Mg_{1/3}Mn_{2/3}O_2$ upon the same amount of electrochemical charge transfer. This is again expected because mRIXS detects only the lattice O redox, without contributions from the oxygen release and surface reactions that have been reported in many previous works for Li-rich electrodes.[28,35,55–58] As a very rough estimation, if we ignore the different TM-O hybridization background in the two systems that affect the absolute sPFY intensity of the 529.7 eV peak after scaling (see Experimental Procedures), lattice O-redox contribution could be estimated to be about 70% (0.55/0.77) of the total capacity during the initial charge plateau with about 0.38 mol electron transfer. Other capacity contributions mainly including oxygen release thus lead to 0.52–0.38 = 0.14 mol electron transfer, corresponding to about 40 mAh g^{-1}. This is surprisingly consistent with the measured capacity contribution from oxygen release in $Li_{1.2}Ni_{0.2}Mn_{0.6}O_2$ (35 mAh g^{-1}) in our previous work,[33] considering that other surface reactions also contribute to the charge capacity in Li-rich systems.[28,59–61] For the same reason that mRIXS detects only the lattice O redox, although the 76% reversibility seems surprisingly high for a Li-rich system, it is reasonable as this is from distinguished lattice O redox only. The capability of mRIXS technique to distinguish lattice O redox from other irreversible oxygen contributions delivers an important piece of information that lattice O redox itself is not as irreversible as we commonly believe, i.e., the irreversibility of the general O-redox discussion is largely from non-lattice O-redox reactions, not lattice O-redox reactions.

Finally, the good match between spectroscopic quantifications and electrochemical capacity for $Na_{2/3}Mg_{1/3}Mn_{2/3}O_2$ indicates that this system is dominated by stable lattice O redox with limited non-lattice oxygen contributions. This allows reasonable quantifications of the absolute charge-transfer numbers based on the mRIXS-sPFY peak area changes (Figure 7C). It is important to note, however, that such absolute quantification could/should only be performed for systems with negligible non-lattice O-redox reactions, and the conversion ratio between peak area and electron transfer could be material dependent. In a complex system with oxygen release and other oxygen contributions, the peak area change reflects only the lattice O-redox contribution. Therefore, quantitative comparison with electrochemical capacity is relatively more reliable during discharge because most non-lattice oxygen reactions, such as oxygen release, take place during high-voltage charging. Nonetheless, mRIXS-sPFY quantification successfully distinguishes the contributions from lattice O-redox reactions to the electrochemical capacity, and reveals the intrinsic behavior of lattice O redox in the Li-rich systems. Further works remain necessary to uncover the different redox behaviors in many other electrode systems, but the quantifications of the two systems here demonstrate the effectiveness of mRIXS-sPFY to selectively probe the critical lattice O-redox reactions.

Summary and Conclusions

This work firstly introduces two analysis methods to quantify the bulk anionic and cationic redox through the recently developed mRIXS technique. Through the sPFY quantification of the characteristic O-redox feature in O-*K* mRIXS, we demonstrate a reliable quantification of the reversibility of lattice O redox. Through the iPFY extracted from Mn-*L* mRIXS, bulk signals with non-distorted lineshape could be directly fitted for quantitative values of Mn oxidation state concentrations. The

O and Mn redox are thus identified independently and consistently interpret the total electrochemical capacity. More importantly, the reversibility of lattice O redox during the initial cycle, and the cyclability over extended cycles, could be quantified through such photon-in-photon-out bulk probes.

We synthesize a P2-type $Na_{2/3}Mg_{1/3}Mn_{2/3}O_2$ NIB material with nominally only Mn^{4+}. Counterintuitively, such an adjustment improves the initial charge capacity to 162 mAh g^{-1}, higher than the capacity with other stoichiometry in this family. Quantitative analysis of Mn-*L* mRIXS-iPFY shows that only 8 mAh g^{-1} capacity is contributed by the trace amount of Mn^{3+}/Mn^{4+} redox during the initial charge. Almost all the improved charge capacity is from a 4.2-V high-potential plateau with Mn^{4+} throughout the process. In the meantime, the O-*K* mRIXS-sPFY quantification reveals the contrast of the amount of O redox during the initial charge and discharge process, which matches the amount of emerging Mn redox and deciphers the Mn- and O-redox contributions to the total capacity: the improved charge capacity through the 4.2-V plateau is purely from O-redox reactions. During discharge, the initial 0.42 mol Na intercalation is compensated by O-redox reaction and then 0.16 mol Na intercalation is accompanied by Mn redox, in which Mn^{4+} is reduced to Mn^{3+}. The Mn and O redox are well separated in different potential regions in $Na_{2/3}Mg_{1/3}Mn_{2/3}O_2$, as clearly defined by mRIXS data, and the O redox in the initial cycle is 79% reversible.

Over extended cycles, the O redox in $Na_{2/3}Mg_{1/3}Mn_{2/3}O_2$ is highly cyclable until the 50^{th} cycle, and 87% of the O redox is sustained at the 100^{th} cycle, regardless of the disappearance of the charge plateau after only ten cycles. Such a dissociation between the high-voltage plateau and O redox was also observed in Li-rich compounds after the initial cycle,[31] but is now clearly revealed in NIB systems also.[20]

The mRIXS-sPFY quantification established in this work addresses a critical parameter of lattice O redox: the reversibility. The quantification value of $Li_{1.17}Ni_{0.21}Co_{0.08}Mn_{0.54}O_2$ system reveals a decent initial-cycle reversibility of 76% and 44% retention after 500 cycles of the lattice O redox. However, compared with $Na_{2/3}Mg_{1/3}Mn_{2/3}O_2$, the spectroscopic variation from lattice O redox in $Li_{1.17}Ni_{0.21}Co_{0.08}Mn_{0.54}O_2$ is much lower with the same electrochemical charge compensation, due to other oxygen contributions such as oxygen release and surface reactions. Therefore, mRIXS-sPFY analysis successfully distinguishes the lattice O redox from other capacity contributions in complex systems with various redox-active oxygen activities.

This work establishes a reliable benchmark and methodology for quantifying the reversibility of lattice O redox in bulk electrodes. Being able to distinguish and quantify the lattice O redox from other oxygen contributions through mRIXS enables analysis of the intrinsic lattice O-redox behaviors. While we focus on quantifying only the reversibility of lattice O redox in this work, more sophisticated mRIXS analysis could potentially reach an absolute amount of O-redox contributions based on reliable references and fundamental understandings of mRIXS-sPFY lineshape, an important technical topic to pursue in the future. Scientifically, direct experimental evidence of the highly reversible and cyclable lattice O redox provides optimism for improving 3*d* TM-based electrode materials for both LIBs and NIBs. The combined quantification results of both cationic and anionic redox reactions not only provide direct experimental verifications that electrochemically inactive dopants, e.g., Mg or Li, suppress the TM redox and enable reversible lattice O redox,[62] more importantly it also shows that mRIXS is powerful for evaluating other and

detailed material optimizations toward reversible lattice O redox in future works, e.g., the difference between Mg and Li dopants. In addition, the similar mRIXS feature in the LIB and NIB electrodes indicates a common O-redox mechanism that is yet to be uncovered. The comparison between the two different systems implies the importance of distinguishing lattice O redox from other oxygen activities for revealing the intrinsic properties of the practically meaningful lattice O-redox activities.

EXPERIMENTAL PROCEDURES

$Na_{2/3}Mg_{1/3}Mn_{2/3}O_2$ Synthesis

$Na_{2/3}Mg_{1/3}Mn_{2/3}O_2$ was prepared by a PVP-assisted gel combustion method.[49,50] Stoichiometric $NaOAc{\cdot}4H_2O$, $Mg(OAc)_2{\cdot}4H_2O$, and $Mn(OAc)_2{\cdot}4H_2O$, and PVP (the molar ratio of PVP monomer to total metal ions was 2.0) were dissolved in deionized water and pH 3 was achieved by adding 1:1 HNO_3. The mixture was stirred at 120°C to obtain dried gel. The dried gel was ignited on a hot plate to induce a combustion process, which lasted for several minutes. The resulting precursor was preheated at 400°C for 2 hr and then calcined at 900°C for 6 hr with the heating rate of 5°C min^{-1}. After heat treatment, the oven was switched off and the sample was cooled down naturally. The whole process was performed in air. The control of the final stoichiometry is consistent with and directly confirmed by the electrochemical and spectroscopic results throughout this work.

Morphology and Crystal Structure Characterization

The morphology was examined using a JEOL 7500F scanning electron microscope. The analysis of the phase purity and the structural characterization were made by XRD using a Bruker D2 PHASER diffractometer equipped with Cu Kα radiation.

Electrochemical Tests

The $Na_{2/3}Mg_{1/3}Mn_{2/3}O_2$ cathode was prepared by mixing 80 wt% active material, 10 wt% acetylene black, and 10 wt% polyvinylidene fluoride binder in N-methylpyrrolidone to form a slurry. The slurry was doctor-bladed onto aluminum foil, dried at 60°C, and punched into electrode discs with a diameter of 12.7 mm. The prepared electrodes were dried at 130°C for 12 hr in a vacuum oven and show typically an active material loading of about 4 mg cm^{-2}. The electrochemical cells were fabricated with the $Na_{2/3}Mg_{1/3}Mn_{2/3}O_2$ cathode, sodium foil anode, 1 mol L^{-1} $NaClO_4$ in propylene carbonate as electrolyte, and double-layered glass fiber as separator in an argon-filled glovebox. Electrochemical performances were evaluated using CR2325 coin cells. Galvanostatic charge-discharge tests were performed using Maccor 4000.

$Li_{1.17}Ni_{0.21}Co_{0.08}Mn_{0.54}O_2$

The preparation, morphology, and structure characterization, and electrochemical tests of $Li_{1.17}Ni_{0.21}Co_{0.08}Mn_{0.54}O_2$, were described previously by Gent et al.[31]

Soft X-Ray Absorption Spectroscopy

Soft XAS was performed in the iRIXS endstation at Beamline 8.0.1 of the Advanced Light Source (ALS) at Lawrence Berkeley National Laboratory.[30] For all the samples in the first cycle, $Na_{2/3}Mg_{1/3}Mn_{2/3}O_2$ cathodes were electrochemically cycled to the representative SoC at rate of 0.1 C in Swagelok cells. For the samples at $n \geq 10$ cycles, the cathodes were charged and discharged for $n - 1$ cycles at 1 C and then were electrochemically cycled to the representative SoC at 0.1 C. The combination of different rates prevents the leakage of Swagelok cells during long-time running and ensures the accurate SoC. Electrodes were disassembled and rinsed

immediately with dimethyl carbonate thoroughly to lock the SoC and remove surface residue. The electrodes were then loaded into our special sample transfer chamber inside the Ar glovebox. The sample transfer chamber was sealed and mounted onto the load lock of the XAS endstation for direct pump-down to avoid any air exposure effects. XAS data were collected from the side of the electrodes facing current collector in both TEY and TFY modes. All the spectra were normalized to the beam flux measured by the upstream gold mesh. The experimental energy resolution was 0.15 eV without considering core-hole lifetime broadening.

Mapping of Resonant Inelastic X-Ray Scattering

mRIXS measurements were performed in iRIXS endstation at Beamline 8.0.1 of the ALS.[30] Data were collected through the ultra-high-efficiency modular spectrometer.[63] The resolution of the excitation energy is about 0.35 eV and the emission energy about 0.25 eV. An excitation energy step size of 0.2 eV was chosen for all maps. mRIXS were collected at each excitation energy. Final 2D images were obtained through a data process involving normalization to the beam flux and collection time, integration, and combination, which has been detailed previously.[64]

iPFY and sPFY Quantifications

Mn-*L* iPFY spectra are obtained by formula iPFY = a/$PFY_{O\text{-}K}$ ("a" is a normalization coefficient). $PFY_{O\text{-}K}$ is obtained by integrating the Mn-*L* mRIXS by integrating the intensity across the emission-energy range from 495 to 510 eV with excitation energy scanning through the Mn-*L* edges. Principles of iPFY have been explained before and briefed in this work.[30,41] Quantitative fittings of Mn-*L* iPFY follows our established linear combination method with three standard experimental spectra.[39]

The O-*K* sPFY signal was extracted by integrating the mRIXS intensity across the emission-energy range from 522.8 to 523.8 eV. This mRIXS feature has been established to be the characteristic energy range of O-redox activities.[20,31,33] For quantitative analysis, the spectra were scaled to the 529.7-eV peak. The area of O-*K* sPFY 531-eV peak was integrated from 530.2 to 532 eV. For the cyclability analysis of extended cycles, the sPFY 531-eV peak area change is calculated by the difference between the fully charged and discharged states at the 1^{st}, 10^{th}, 50^{th}, and 100^{th} cycles. We note that different spectral normalization does not change the conclusions in this work, because the quantified values of reversibility and cyclability only depends on the intensity contrasts (changes) of the characteristic O-redox features. Such a comparative intensity change could be seen directly with the sPFY raw data plots.

SUPPLEMENTAL INFORMATION

Supplemental Information includes 12 figures and can be found with this article online at https://doi.org/10.1016/j.joule.2018.11.014.

ACKNOWLEDGMENTS

The Advanced Light Source is supported by the Director, Office of Science, Office of Basic Energy Sciences, of the US Department of Energy under contract no. DE-AC02-05CH11231. We also acknowledge the support from the Fundamental Research Funds for the Central Universities of China (N150204017), the National Natural Science Foundation of China (U1504521, 51604224), Science and Technology on Reliability Physics and Application of Electronic Component Laboratory open fund (ZHD201605), and Assistant Secretary for Energy Efficiency and Renewal Energy under the Battery Materials Research program under contract no.

DE-AC02-05CH11231. Q.L. and S.Y. acknowledge financial support from the China Scholarship Council through 111 project no. B13029. W.Y. acknowledges the support from the Energy Biosciences Institute through the EBI-Shell program on analyzing the Li-rich results. Z.Z. and S.S. thank the financial support of ALS doctoral fellowship.

AUTHOR CONTRIBUTIONS

K.D., G.L., and W.Y. conceived the project and coordinated the collaboration with contributions from all authors. K.D., J.M., G.A., C.S., Z.L., and G.L. synthesized the $Na_{2/3}Mg_{1/3}Mn_{2/3}O_2$ material and performed structural and electrochemical characterizations. K.D., J.W., Z.Z., Q.L., S.S., L.F.J.P., Y.-d.C., and W.Y. performed spectroscopic experiments. W.E.G. and W.C.C. studied Li-rich materials. K.D. and W.Y. analyzed the results and prepared the manuscript with input from all authors.

DECLARATION OF INTERESTS

The authors declare no competing interests.

Received: July 21, 2018
Revised: October 20, 2018
Accepted: November 14, 2018
Published: December 12, 2018

REFERENCES

1. Goodenough, J.B., and Park, K.-S. (2013). The Li-Ion rechargeable battery: a perspective. J. Am. Chem. Soc. *135*, 1167–1176.

2. Grimaud, A., Hong, W.T., Shao-Horn, Y., and Tarascon, J.M. (2016). Anionic redox processes for electrochemical devices. Nat. Mater. *15*, 121–126.

3. McCalla, E., Abakumov, A.M., Saubanère, M., Foix, D., Berg, E.J., Rousse, G., Doublet, M.-L., Gonbeau, D., Novák, P., and Van Tendeloo, G. (2015). Visualization of OO peroxo-like dimers in high-capacity layered oxides for Li-ion batteries. Science *350*, 1516–1521.

4. Sathiya, M., Rousse, G., Ramesha, K., Laisa, C.P., Vezin, H., Sougrati, M.T., Doublet, M.L., Foix, D., Gonbeau, D., Walker, W., et al. (2013). Reversible anionic redox chemistry in high-capacity layered-oxide electrodes. Nat. Mater. *12*, 827–835.

5. Luo, K., Roberts, M.R., Hao, R., Guerrini, N., Pickup, D.M., Liu, Y.S., Edstrom, K., Guo, J., Chadwick, A.V., Duda, L.C., et al. (2016). Charge-compensation in 3d-transition-metal-oxide intercalation cathodes through the generation of localized electron holes on oxygen. Nat. Chem. *8*, 684–691.

6. Seo, D.H., Lee, J., Urban, A., Malik, R., Kang, S., and Ceder, G. (2016). The structural and chemical origin of the oxygen redox activity in layered and cation-disordered Li-excess cathode materials. Nat. Chem. *8*, 692–697.

7. Okubo, M., and Yamada, A. (2017). Molecular orbital principles of oxygen-redox battery electrodes. ACS Appl. Mater. Interfaces *9*, 36463–36472.

8. Assat, G., and Tarascon, J.-M. (2018). Fundamental understanding and practical challenges of anionic redox activity in Li-ion batteries. Nat. Energy *3*, 373–386.

9. Yabuuchi, N. (2017). Solid-state redox reaction of oxide ions for rechargeable batteries. Chem. Lett. *46*, 412–422.

10. Rozier, P., Sathiya, M., Paulraj, A.-R., Foix, D., Desaunay, T., Taberna, P.-L., Simon, P., and Tarascon, J.-M. (2015). Anionic redox chemistry in Na-rich $Na_2Ru_{1-y}Sn_yO_3$ positive electrode material for Na-ion batteries. Electrochem. Commun. *53*, 29–32.

11. Perez, A.J., Batuk, D., Saubanère, M., Rousse, G., Foix, D., McCalla, E., Berg, E.J., Dugas, R., van den Bos, K.H.W., Doublet, M.-L., et al. (2016). Strong oxygen participation in the redox governing the structural and electrochemical properties of Na-rich layered oxide Na_2IrO_3. Chem. Mater. *28*, 8278–8288.

12. Assat, G., Foix, D., Delacourt, C., Iadecola, A., Dedryvère, R., and Tarascon, J.-M. (2017). Fundamental interplay between anionic/cationic redox governing the kinetics and thermodynamics of lithium-rich cathodes. Nat. Commun. *8*, 2219.

13. Luo, K., Roberts, M.R., Guerrini, N., Tapia-Ruiz, N., Hao, R., Massel, F., Pickup, D.M., Ramos, S., Liu, Y.S., Guo, J., et al. (2016). Anion redox chemistry in the cobalt free 3d transition metal oxide intercalation electrode $Li[Li_{0.2}Ni_{0.2}Mn_{0.6}]O_2$. J. Am. Chem. Soc. *138*, 11211–11218.

14. Oishi, M., Yamanaka, K., Watanabe, I., Shimoda, K., Matsunaga, T., Arai, H., Ukyo, Y., Uchimoto, Y., Ogumi, Z., and Ohta, T. (2016). Direct observation of reversible oxygen anion redox reaction in Li-rich manganese oxide, Li_2MnO_3, studied by soft X-ray absorption spectroscopy. J. Mater. Chem. A *4*, 9293–9302.

15. Ma, C., Alvarado, J., Xu, J., Clement, R.J., Kodur, M., Tong, W., Grey, C.P., and Meng, Y.S. (2017). Exploring oxygen activity in the high energy P2-type $Na_{0.78}Ni_{0.23}Mn_{0.69}O_2$ cathode material for Na-Ion batteries. J. Am. Chem. Soc. *139*, 4835–4845.

16. Oishi, M., Yogi, C., Watanabe, I., Ohta, T., Orikasa, Y., Uchimoto, Y., and Ogumi, Z. (2015). Direct observation of reversible charge compensation by oxygen ion in Li-rich manganese layered oxide positive electrode material, $Li_{1.16}Ni_{0.15}Co_{0.19}Mn_{0.50}O_2$. J. Power Sources *276*, 89–94.

17. Yabuuchi, N., Nakayama, M., Takeuchi, M., Komaba, S., Hashimoto, Y., Mukai, T., Shiiba, H., Sato, K., Kobayashi, Y., Nakao, A., et al. (2016). Origin of stabilization and destabilization in solid-state redox reaction of oxide ions for lithium-ion batteries. Nat. Commun. *7*, 13814.

18. Foix, D., Sathiya, M., McCalla, E., Tarascon, J.-M., and Gonbeau, D. (2016). X-ray photoemission spectroscopy study of cationic and anionic redox processes in high-capacity Li-ion battery layered-oxide electrodes. J. Phys. Chem. C *120*, 862–874.

19. Maitra, U., House, R.A., Somerville, J.W., Tapia-Ruiz, N., Lozano, J.G., Guerrini, N., Hao, R., Luo, K., Jin, L., Perez-Osorio, M.A., et al. (2018). Oxygen redox chemistry without excess alkali-metal ions in $Na_{2/3}[Mg_{0.28}Mn_{0.72}]O_2$. Nat. Chem. *10*, 288–295.

20. Yang, W., and Devereaux, T.P. (2018). Anionic and cationic redox and interfaces in batteries: advances from soft X-ray absorption

spectroscopy to resonant inelastic scattering. J. Power Sources *389*, 188–197.

21. Ortiz-Vitoriano, N., Drewett, N.E., Gonzalo, E., and Rojo, T. (2017). High performance manganese-based layered oxide cathodes: overcoming the challenges of sodium ion batteries. Energy Environ. Sci. *10*, 1051–1074.

22. Han, M.H., Gonzalo, E., Singh, G., and Rojo, T. (2015). A comprehensive review of sodium layered oxides: powerful cathodes for Na-ion batteries. Energy Environ. Sci. *8*, 81–102.

23. Xu, J., Lee, D.H., Clément, R.J., Yu, X., Leskes, M., Pell, A.J., Pintacuda, G., Yang, X.-Q., Grey, C.P., and Meng, Y.S. (2014). Identifying the critical role of Li substitution in P2-$Na_x[Li_yNi_zMn_{1-y-z}]O_2$ (0< x, y, z< 1) intercalation cathode materials for high-energy Na-ion batteries. Chem. Mater. *26*, 1260–1269.

24. Clément, R.J., Bruce, P.G., and Grey, C.P. (2015). Review—manganese-based P2-type transition metal oxides as sodium-ion battery cathode materials. J. Electrochem. Soc. *162*, A2589–A2604.

25. Yabuuchi, N., Hara, R., Kajiyama, M., Kubota, K., Ishigaki, T., Hoshikawa, A., and Komaba, S. (2014). New O2/P2-type Li-excess layered manganese oxides as promising multi-functional electrode materials for rechargeable Li/Na batteries. Adv. Energy Mater. *4*, 1301453.

26. Slater, M.D., Kim, D., Lee, E., and Johnson, C.S. (2013). Sodium-ion batteries. Adv. Funct. Mater. *23*, 947–958.

27. Du, K., Zhu, J.Y., Hu, G.R., Gao, H.C., Li, Y.T., and Goodenough, J.B. (2016). Exploring reversible oxidation of oxygen in a manganese oxide. Energy Environ. Sci. *9*, 2575–2577.

28. Renfrew, S.E., and McCloskey, B.D. (2017). Residual lithium carbonate predominantly accounts for first cycle CO_2 and CO outgassing of Li-stoichiometric and Li-rich layered transition-metal oxides. J. Am. Chem. Soc. *139*, 17853–17860.

29. Yang, W. (2018). Oxygen release and oxygen redox. Nat. Energy *3*, 619–620.

30. Qiao, R., Li, Q., Zhuo, Z., Sallis, S., Fuchs, O., Blum, M., Weinhardt, L., Heske, C., Pepper, J., Jones, M., et al. (2017). High-efficiency in situ resonant inelastic x-ray scattering (iRIXS) endstation at the advanced light source. Rev. Sci. Instrum. *88*, 033106.

31. Gent, W.E., Lim, K., Liang, Y., Li, Q., Barnes, T., Ahn, S.-J., Stone, K.H., McIntire, M., Hong, J., Song, J.H., et al. (2017). Strong coupling between bulk oxygen redox and cation migration explains unusual electrochemistry in 3d Li-rich layered oxides. Nat. Commun. *8*, 2091.

32. Firouzi, A., Qiao, R., Motallebi, S., Valencia, C.W., Israel, H.S., Fujimoto, M., Wray, L.A., Chuang, Y.D., Yang, W., and Wessells, C.D. (2018). Monovalent manganese based anodes and co-solvent electrolyte for stable low-cost high-rate sodium-ion batteries. Nat. Commun. *9*, 861.

33. Xu, J., Sun, M., Qiao, R., Renfrew, S.E., Ma, L., Wu, T., Hwang, S., Nordlund, D., Su, D., Amine, K., et al. (2018). Elucidating anionic oxygen activity in lithium-rich layered oxides. Nat. Commun. *9*, 947.

34. Zhuo, Z., Pemmaraju, C.D., Vinson, J., Jia, C., Moritz, B., Lee, I., Sallis, S., Li, Q., Wu, J., Dai, K., et al. (2018). Spectroscopic signature of oxidized oxygen states in peroxides. J. Phys. Chem. Lett. *9*, 6378–6384.

35. Strehle, B., Kleiner, K., Jung, R., Chesneau, F., Mendez, M., Gasteiger, H.A., and Piana, M. (2017). The role of oxygen release from Li-and Mn-rich layered oxides during the first cycles investigated by on-line electrochemical mass spectrometry. J. Electrochem. Soc. *164*, A400–A406.

36. Zhan, C., Yao, Z., Lu, J., Ma, L., Maroni, V.A., Li, L., Lee, E., Alp, E.E., Wu, T., Wen, J., et al. (2017). Enabling the high capacity of lithium-rich anti-fluorite lithium iron oxide by simultaneous anionic and cationic redox. Nat. Energy *2*, 963–971.

37. Lin, F., Liu, Y., Yu, X., Cheng, L., Singer, A., Shpyrko, O.G., Xin, H.L., Tamura, N., Tian, C., Weng, T.C., et al. (2017). Synchrotron X-ray analytical techniques for studying materials electrochemistry in rechargeable batteries. Chem. Rev. *117*, 13123–13186.

38. Yang, W., Liu, X., Qiao, R., Olalde-Velasco, P., Spear, J.D., Roseguo, L., Pepper, J.X., Chuang, Y.-D., Denlinger, J.D., and Hussain, Z. (2013). Key electronic states in lithium battery materials probed by soft X-ray spectroscopy. J. Electron Spectros. Relat. Phenomena *190*, 64–74.

39. Li, Q., Qiao, R., Wray, L.A., Chen, J., Zhuo, Z., Chen, Y., Yan, S., Pan, F., Hussain, Z., and Yang, W. (2016). Quantitative probe of the transition metal redox in battery electrodes through soft x-ray absorption spectroscopy. J. Phys. D Appl. Phys. *49*, 413003.

40. Wu, J., Song, J., Dai, K., Zhuo, Z., Wray, L.A., Liu, G., Shen, Z.X., Zeng, R., Lu, Y., and Yang, W. (2017). Modification of transition-metal redox by interstitial water in hexacyanometalate electrodes for sodium-ion batteries. J. Am. Chem. Soc. *139*, 18358–18364.

41. Achkar, A.J., Regier, T.Z., Wadati, H., Kim, Y.J., Zhang, H., and Hawthorn, D.G. (2011). Bulk sensitive x-ray absorption spectroscopy free of self-absorption effects. Phys. Rev. B *83*, 081106.

42. Qiao, R., Wray, L.A., Kim, J.-H., Pieczonka, N.P.W., Harris, S.J., and Yang, W. (2015). Direct experimental probe of the Ni(II)/Ni(III)/Ni(IV) redox evolution in $LiNi_{0.5}Mn_{1.5}O_4$ electrodes. J. Phys. Chem. C *119*, 27228–27233.

43. Yabuuchi, N., Hara, R., Kubota, K., Paulsen, J., Kumakura, S., and Komaba, S. (2014). A new electrode material for rechargeable sodium batteries: P2-type $Na_{2/3}[Mg_{0.28}Mn_{0.72}]O_2$ with anomalously high reversible capacity. J. Mater. Chem. A *2*, 16851–16855.

44. Hu, E., Yu, X., Lin, R., Bi, X., Lu, J., Bak, S., Nam, K.-W., Xin, H.L., Jaye, C., Fischer, D.A., et al. (2018). Evolution of redox couples in Li- and Mn-rich cathode materials and mitigation of voltage fade by reducing oxygen release. Nat. Energy *3*, 690–698.

45. Butorin, S.M., Guo, J., Wassdahl, N., and Nordgren, E.J. (2000). Tunable-excitation soft X-ray fluorescence spectroscopy of high-Tc superconductors: an inequivalent-site seeing story. J. Electron Spectrosc. *110-111*, 235–273.

46. Glans, P., Gunnelin, K., Skytt, P., Guo, J., Wassdahl, N., Nordgren, J., Agren, H., Gel'mukhanov, F.K., Warwick, T., and Rotenberg, E. (1996). Resonant x-ray emission spectroscopy of molecular oxygen. Phys. Rev. Lett. *76*, 2448–2451.

47. Qiao, R., Chuang, Y.D., Yan, S., and Yang, W. (2012). Soft x-ray irradiation effects of Li_2O_2, Li_2CO_3 and Li_2O revealed by absorption spectroscopy. PLoS One *7*, e49182.

48. Qiao, R., Chin, T., Harris, S.J., Yan, S., and Yang, W. (2013). Spectroscopic fingerprints of valence and spin states in manganese oxides and fluorides. Curr. Appl. Phys. *13*, 544–548.

49. Dai, K., Mao, J., Song, X., Battaglia, V., and Liu, G. (2015). $Na_{0.44}MnO_2$ with very fast sodium diffusion and stable cycling synthesized via polyvinylpyrrolidone-combustion method. J. Power Sources *285*, 161–168.

50. Dai, K., Mao, J., Li, Z., Zhai, Y., Wang, Z., Song, X., Battaglia, V., and Liu, G. (2014). Microsized single-crystal spinel LAMO for high-power lithium ion batteries synthesized via polyvinylpyrrolidone combustion method. J. Power Sources *248*, 22–27.

51. Paulsen, J.M., Donaberger, R.A., and Dahn, J.R. (2000). Layered T2-, O6-, O2-, and P2-type $A_{2/3}[M'^{2+}_{1/3}M^{4+}_{2/3}]O_2$ bronzes, A = Li, Na; M′ = Ni, Mg; M = Mn, Ti. Chem. Mater. *12*, 2257–2267.

52. Qiao, R., Wang, Y., Olalde-Velasco, P., Li, H., Hu, Y.-S., and Yang, W. (2015). Direct evidence of gradient Mn(II) evolution at charged states in $LiNi_{0.5}Mn_{1.5}O_4$ electrodes with capacity fading. J. Power Sources *273*, 1120–1126.

53. Qiao, R., Dai, K., Mao, J., Weng, T.-C., Sokaras, D., Nordlund, D., Song, X., Battaglia, V.S., Hussain, Z., Liu, G., et al. (2015). Revealing and suppressing surface Mn(II) formation of $Na_{0.44}MnO_2$ electrodes for Na-ion batteries. Nano Energy *16*, 186–195.

54. Liu, X., Wang, Y.J., Barbiellini, B., Hafiz, H., Basak, S., Liu, J., Richardson, T., Shu, G., Chou, F., Weng, T.C., et al. (2015). Why $LiFePO_4$ is a safe battery electrode: Coulomb repulsion induced electron-state reshuffling upon lithiation. Phys. Chem. Chem. Phys. *17*, 26369–26377.

55. Saubanère, M., McCalla, E., Tarascon, J.-M., and Doublet, M.-L. (2016). The intriguing question of anionic redox in high-energy density cathodes for Li-ion batteries. Energy Environ. Sci. *9*, 984–991.

56. Hy, S., Felix, F., Rick, J., Su, W.-N., and Hwang, B.J. (2014). Direct in situ observation of Li_2O evolution on Li-rich high-capacity cathode material, $Li[Ni_xLi_{(1-2x)/3}Mn_{(2-x)/3}]O_2$ ($0 \leq x \leq 0.5$). J. Am. Chem. Soc. *136*, 999–1007.

57. McCalla, E., Sougrati, M.T., Rousse, G., Berg, E.J., Abakumov, A., Recham, N., Ramesha, K., Sathiya, M., Dominko, R., Van Tendeloo, G., et al. (2015). Understanding the roles of anionic redox and oxygen release during electrochemical cycling of lithium-rich layered Li_4FeSbO_6. J. Am. Chem. Soc. *137*, 4804–4814.

58. Armstrong, A.R., Holzapfel, M., Novák, P., Johnson, C.S., Kang, S.-H., Thackeray, M.M., and Bruce, P.G. (2006). Demonstrating oxygen loss and associated structural reorganization in

the lithium battery cathode $Li[Ni_{0.2}Li_{0.2}Mn_{0.6}]O_2$. J. Am. Chem. Soc. *128*, 8694–8698.

59. Qiu, B., Zhang, M., Wu, L., Wang, J., Xia, Y., Qian, D., Liu, H., Hy, S., Chen, Y., An, K., et al. (2016). Gas–solid interfacial modification of oxygen activity in layered oxide cathodes for lithium-ion batteries. Nat. Commun. *7*, 12108.

60. Liu, Y., Yang, Z., Li, J., Niu, B., Yang, K., and Kang, F. (2018). A novel surface-heterostructured $Li_{1.2}Mn_{0.54}Ni_{0.13}Co_{0.13}O_2@Ce_{0.8}Sn_{0.2}O_{2-\sigma}$ cathode material for Li-ion batteries with improved initial irreversible capacity loss. J. Mater. Chem. A *6*, 13883–13893.

61. Wu, B., Yang, X., Jiang, X., Zhang, Y., Shu, H., Gao, P., Liu, L., and Wang, X. (2018). Synchronous tailoring surface structure and chemical composition of Li-rich–layered oxide for high-energy lithium-ion batteries. Adv. Funct. Mater. *28*, 1803392.

62. Yabuuchi, N., Kubota, K., Dahbi, M., and Komaba, S. (2014). Research development on sodium-ion batteries. Chem. Rev. *114*, 11636–11682.

63. Chuang, Y.-D., Shao, Y.-C., Cruz, A., Hanzel, K., Brown, A., Frano, A., Qiao, R., Smith, B., Domning, E., Huang, S.-W., et al. (2017). Modular soft x-ray spectrometer for applications in energy sciences and quantum materials. Rev. Sci. Instrum. *88*, 013110.

64. Wu, J., Sallis, S., Qiao, R., Li, Q., Zhuo, Z., Dai, K., Guo, Z., and Yang, W. (2018). Elemental-sensitive detection of the chemistry in batteries through soft x-ray absorption spectroscopy and resonant inelastic x-ray scattering. J. Vis. Exp. *134*, e57415.